Eur. Phys. J. Plus (2026) 141:798
https://doi.org/10.1140/epjp/s13360-026-07974-1

THE EUROPEAN PHYSICAL JOURNAL PLUS

Regular Article

A doublet mechanics approach to torsional vibration in viscoelastic short fiber–reinforced nanotubes

Murat Akpınar[1,a], **Hayrullah Gün Kadıoğlu**[2,b], **Mustafa Özgür Yaylı**[1,c]

[1] Department of Civil Engineering, Engineering Faculty, Bursa Uludag University, Görükle Campus, 16059 Bursa, Turkey
[2] Department of Construction, Technical Sciences Vocational School, İstanbul Arel University, Tepekent Campus, 34537 Istanbul, Turkey

Received: 24 March 2026 / Accepted: 15 June 2026
© The Author(s) 2026

Abstract This study investigates the torsional vibration behavior of short fiber–reinforced (SFRC) nanotubes within the framework of doublet mechanics (DM) theory, while also accounting for viscoelastic material effects and flexible boundary conditions (BCs). The effective mechanical properties of the composite are estimated through the Halpin–Tsai nanomechanical model, and the Kelvin–Voigt approach is adopted to represent viscoelastic damping. A semi-analytical solution is developed by expressing the rotation field as a Fourier sine series and applying Stokes' transformation, which enables the treatment of elastic torsional spring BCs in a unified manner. A key advantage of the proposed formulation is its flexibility: any combination of BCs—from fully clamped to completely free—can be handled simply by adjusting the spring stiffnesses without reformulating the governing equations. Numerical results reveal that damping has a significant effect on natural frequencies, particularly in higher vibration modes, where it can strongly suppress the dynamic response. Increasing the fiber volume fraction and aspect ratio enhances torsional stiffness and raises the frequencies, while a higher fiber-to-matrix mass density ratio leads to a slight decrease. The findings highlight the complex interplay between damping, scale effects, and nanostructural parameters, demonstrating that DM provides a robust higher-grade continuum framework for the dynamic analysis of reinforced nanostructures.

1 Introduction

Continuum mechanics has traditionally served as the primary theoretical basis for understanding the mechanical and dynamic behavior of engineering structures. In particular, at the macroscopic level, classical (local) elasticity theory has been widely used to analyze problems such as deformation, vibration, stability, and wave propagation in beams, rods, and similar structural components. According to this theory, the stress at a given material point depends only on the strain at that same point, meaning that no intrinsic material length scale is included in the formulation [1]. For structures with conventional dimensions, this assumption generally provides sufficiently accurate results and has therefore been adopted in most classical analyses. However, as research has increasingly shifted toward micro- and nano-scale systems, it has become clear that this approach is not always adequate. Experimental findings at these smaller scales indicate pronounced size-dependent mechanical responses that cannot be captured by classical elasticity alone. As the structural dimensions become comparable to the internal length scales of the material, the influence of microstructural interactions and long-range forces becomes much more significant.

To capture small-scale effects consistently, DM, a scale-dependent continuum theory, was introduced by Granik [2]. Unlike phenomenological modifications of classical elasticity, DM is based on a microstructural representation in which the material is idealized as interacting particle doublets [3, 4]. This formulation naturally incorporates characteristic length parameters and enables the consistent representation of scale effects arising from microstructural interactions. In this context, Kojić et al. [5] investigated the computational modeling of microstructured solids by reformulating the DM theory within a finite element framework. Fatahi-Vajari and Imam, in their first study [6], examined the axial vibration of single-walled carbon nanotubes (SWCNTs) utilizing DM, and later in their subsequent work [7], extended the formulation to the torsional vibration mode by including both scale and chiral effects. Eltaher et al. [8] investigated the nonlinear stability and vibration behavior of perfect and imperfect SWCNTs in pre- and post-buckling domains by employing the DM theory with Euler–Bernoulli kinematics and nonlinear mid-plane stretching. Yayli and Asa [9] presented an analytical model for free axial vibration of SWCNTs with axial spring restraints using the DM theory, employing Fourier sine series and Stokes' transformation to handle BCs. Civalek et al. [10–12] analyzed nanoscale structures with deformable BCs using DM theory, addressing buckling of nanobeams [10], free longitudinal vibration of functionally graded (FG)

[a] e-mail: muratakpinar@uludag.edu.tr (corresponding author)
[b] e-mail: hayrullahgunkadioglu@arel.edu.tr
[c] e-mail: ozguryayli@uludag.edu.tr

Published online: 10 July 2026

nanorods [11], and torsional vibrations of porous nanorods [12]. Ebrahimian et al. [13] examined the torsional behavior of nanotubes embedded in an elastic medium using DM theory. Azimzadeh et al. [14] analyzed the coupled axial–radial vibration of SWCNTs using DM theory. Kadıoğlu and Yaylı [15] studied the torsional oscillation of FG viscoelastic nanotubes under viscoelastic BCs using DM theory. Eltaher et al. [16] examined the static and dynamic response of geometrically imperfect carbon nanotubes under various BCs using DM theory combined with Euler–Bernoulli kinematics. Karamanli [17] investigated the bending, vibration, and buckling behaviors of zigzag and armchair carbon nanotube-based nanobeams using DM in conjunction with a third-order shear deformation theory and finite element method.

Furthermore, several studies by Gul and Aydogdu have explored the application of DM to static and dynamic analyses, such as statics, buckling, vibration, and wave propagation of nanorods and nanobeams using classical rod and Euler–Bernoulli theories [18]; free vibration and buckling of double-walled carbon nanotubes (DWCNTs) embedded in an elastic medium [19]; longitudinal vibration of nanorods taking into account lateral inertia effects based on Love's assumption [20]; bending, buckling and vibration of micro-nano Timoshenko beams [21]; buckling analysis of FG nanobeams with periodic lattice structures [22]; transverse wave propagation in SWCNTs and DWCNTs [23]; vibration of layered FG nanobeams [24]; axial vibration of nanorods with FEM formulations [25]; vibration of FG periodic nanobeams [26]; hygro-thermal vibration of porous FG nanobeams [27]; free and forced longitudinal vibration of double nanorods [28]; buckling of double nanofibers embedded in elastic matrices [29]; and axial deformation and bending of nanorods and nanobeams with periodic nanostructures [30]. Additionally, Gul et al. [31, 32] investigated the mechanical behavior of nanotubes and nanorods embedded in an elastic medium using DM theory, addressing vibration and buckling characteristics in one study [31] and axial vibration of carbon nanotubes under various BCs in another [32]. In addition to these studies, investigations on bending [33–36], free vibration [37–44], forced vibration [45–47], buckling [48–50], torsional vibration [51–53], and axial vibration [54, 55] of nanostructures are also reported in the literature.

Previous studies have mostly modeled nanostructures as homogeneous, FG, or porous materials. However, limiting the material description to these idealizations does not fully reflect current design approaches. In recent years, increasing attention has been directed toward enhancing the mechanical performance of nanostructures through various composite reinforcement techniques. Within this context, a number of studies have examined the mechanical behavior of different reinforced systems, including SFRC [56–60], carbon nanotube–reinforced [61–65], and graphene platelet–reinforced [66–71] nanostructures.

In addition to material composition and reinforcement, accurately capturing energy dissipation is also essential for realistic modeling of nanostructures. At small scales, damping behavior can differ noticeably from that of bulk materials, especially in polymer-based matrices and composite systems. For this reason, viscoelastic constitutive models are commonly adopted to represent time-dependent responses and internal damping effects. Among these, the Kelvin–Voigt model [72–78] is widely used, while some studies consider both Kelvin–Voigt and Maxwell models together to provide a more comprehensive description of viscoelastic behaviour [79–82].

Although a large number of studies have examined the torsional vibration of nanostructures, most of them are restricted to idealized BCs and classical continuum models. In this respect, DM theory provides a more refined framework, as it incorporates intrinsic length scale parameters that account for the underlying nanostructure, making it particularly suitable for composite materials. Another point that is often overlooked is the role of viscoelastic damping. In nanocomposites, damping can have a noticeable influence on both energy dissipation and overall dynamic response, and neglecting it may lead to less realistic predictions. Motivated by these considerations, the present study develops a unified semi-analytical model for the torsional vibration of SFRC nanotubes within the framework of DM theory. The formulation includes both viscoelastic effects and deformable torsional spring BCs. A general solution is constructed using a Fourier sine series together with Stokes' transformation, which makes it possible to represent different levels of boundary flexibility without the need to re-derive the solution methodology for each specific support condition.

A key advantage of the formulation is the ease with which different BCs can be implemented; simply by adjusting the torsional spring stiffnesses, any case from fully clamped to completely free can be obtained without re-deriving the governing equations. This feature makes the model particularly suitable for nanoelectromechanical systems (NEMS) and nano-sensor applications. Furthermore, the viscoelastic damping framework can enable realistic prediction of energy dissipation in polymer-based nanocomposites, which is essential for the design of high-performance nanoresonators and energy harvesting devices.

2 Mechanical property estimation of SFRC nanotubes via Halpin–Tsai model

In this study, the torsional vibration characteristics of SFRC nanotubes are investigated. The nanotubes are embedded in a matrix with randomly oriented short fibers, as shown in Fig. 1. To reflect the influence of the short fibers, the composite's effective mechanical properties are calculated with the Halpin–Tsai model. In particular, the longitudinal and transverse elastic moduli of the composite, E_L and E_T are calculated using the following expressions [83]:

$$E_L = E_m\left(\frac{1+\left(\frac{2l}{d}\right)\varrho_L V_f}{1-\varrho_L V_f}\right) \tag{1}$$

$$E_T = E_m\left(\frac{1+2\varrho_T V_f}{1-\varrho_T V_f}\right) \tag{2}$$

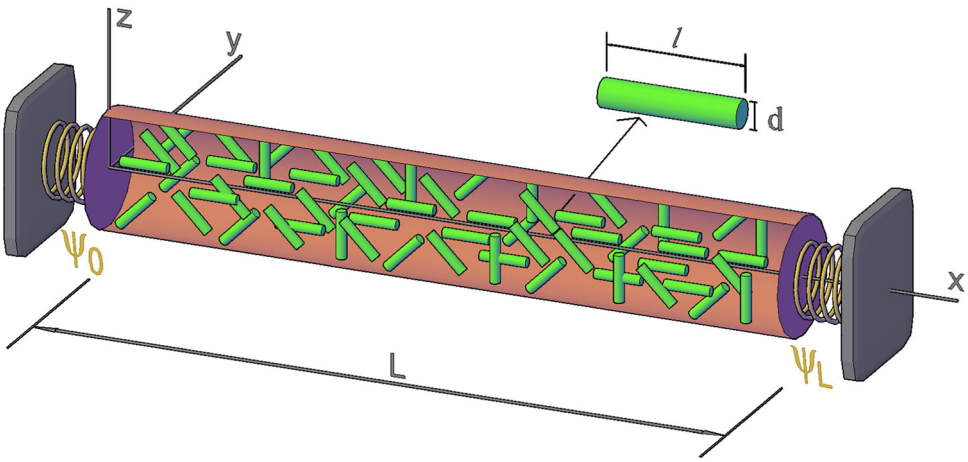


Fig. 1 Model of a SFRC nanotube constrained by torsional springs at both ends

where,

$$\varrho_L = \left(\frac{\frac{E_f}{E_m} - 1}{\frac{E_f}{E_m} + 2\left(\frac{l}{d}\right)} \right) \tag{3}$$

$$\varrho_T = \left(\frac{\frac{E_f}{E_m} - 1}{\frac{E_f}{E_m} + 2} \right) \tag{4}$$

Here, E_m and E_f denote the elastic moduli of the matrix and the short fibers, respectively, while l, d, and V_f represent the fiber length, diameter, and volume fraction. Based on these parameters, the elastic modulus of the composite, E_c, is determined using the following formulation [83]:

$$E_c = \frac{3}{8} E_{_L} + \frac{5}{8} E_{_T} \tag{5}$$

The mass density of the SFRC nanotube, ρ_c, is subsequently determined based on the properties of the matrix (ρ_m) and fibers $\left(\rho_f\right)$ using the following relation [84]:

$$\rho_c = \rho_m \left(1 - V_f\right) + \rho_f V_f \tag{6}$$

We note that direct experimental fabrication of SFRC nanotubes remains a challenge, and the present study is theoretical in nature. However, the concept of nanoscale reinforcement with randomly oriented fibers is supported by the existing literature on CNT- and GPL-reinforced nanocomposites, and the random orientation assumption adopted here offers a more practical pathway for manufacturing compared to perfectly aligned models.

3 Derivation of the theoretical equations based on DM theory

In this section, the theoretical framework is developed within the scope of DM theory. Unlike phenomenological non-classical theories, the size-dependent response in DM emerges directly from the microstructural doublet spacing and the higher-order gradient terms in the strain expansion. In the model, each material atom is represented as a nodal point, as illustrated in Fig. 2. The incremental displacement vector is then formulated as follows [4]:

$$\Delta u_a = u(x + \delta_a^0, t) - u(x, t) \tag{7}$$

Here, u, t, a and x denote the displacement, time, doublet number ($a = 1, 2, 3 \ldots$), and position vector, respectively. Within the DM framework, three types of micro-stresses arise during deformation, as illustrated in Fig. 3: elongation (p_a), torsion (m_a), and shear (t_a). For the current study, torsional and shear deformations are considered negligible, allowing the stresses and strains to be determined primarily from elongation. Since the relative displacement field remains small compared to the separation distance, the unit vector retains its initial form, i.e., $e_a = e_a^0$. Additionally, microstructural deformation is described through the micro-strain ϵ_a, given by [4]:

$$\epsilon_a = \frac{e_a^0 \Delta u_a}{\mu_a} \tag{8}$$

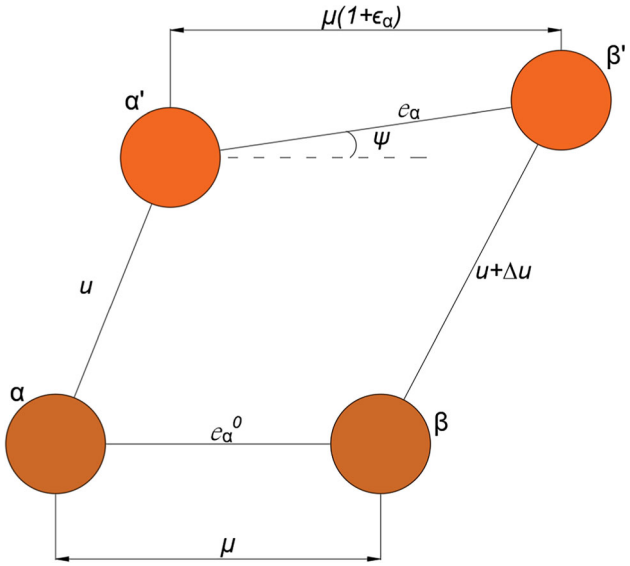


Fig. 2 Deformation behavior observed at the doublet nodes

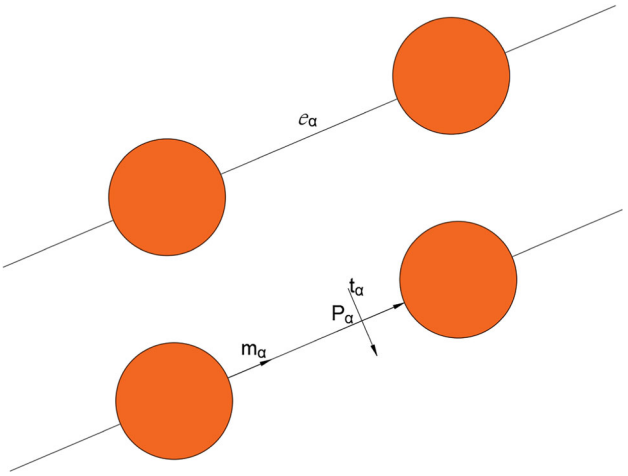


Fig. 3 A schematic representation showing the orientation of the doublet axis

Here, $\mu_a = \mu$ denotes the separation distance between two adjacent doublet points. Using a Taylor series expansion, ϵ_a can be reformulated as [4]:

$$\epsilon_a = \sum_{x=1}^{k} \frac{(\mu_a)^{x-1}}{x!} e_a^0 \left(e_a^0 \nabla\right)^x u \tag{9}$$

In this expression, ∇ represents the Del operator. The micro-stress in the a doublet (p_a) is related to the micro-strain in the β doublet $\left(\epsilon_\beta\right)$ through the following relation [4]:

$$p_a = \sum_{\beta=1}^{d} A_{a\beta} \epsilon_\beta \tag{10}$$

where p_a is the axial micro-stress component and $A_{a\beta}$ refers to the micro-modulus matrix. The unit vector e_a^0 can also be expressed in terms of its components as $e_a^0 = e_{aj}^0 t_j$, where e_{aj}^0 denotes the direction cosines between the doublet orientation and the coordinate axes, and t_j represents the base vectors of the coordinate system. For an isotropic and homogeneous medium with interactions restricted to the local direction, Eq. (10) reduces to the following form [4]:

$$p_a = A_0 \epsilon_a \tag{11}$$

Here, A_0 denotes the stiffness. The macro-stress σ can be expressed in terms of the micro-stress p_a as follows [31, 54]:

$$\sigma = \sum_{a=1}^{d} e_a^0 e_a^0 \sum_{x=1}^{k} \frac{(-\mu_a)^{x-1}}{x!} e_a^0 \left(e_a^0 \nabla\right)^{x-1} p_a \tag{12}$$

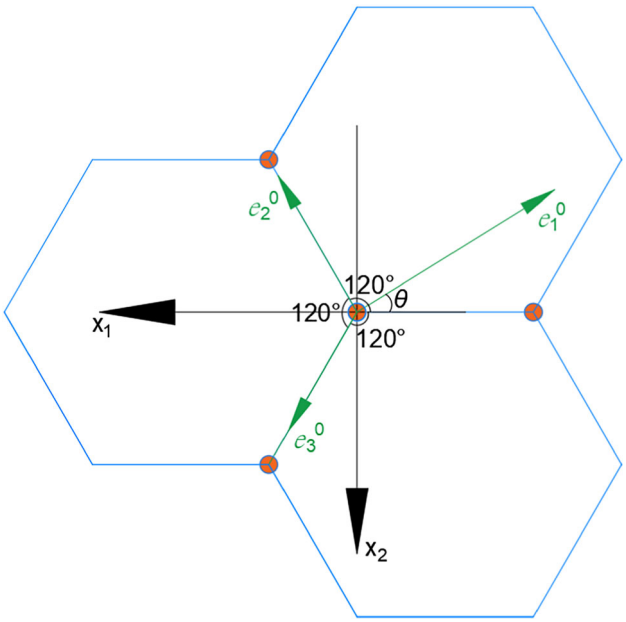


Fig. 4 Alignment of three doublet points within the carbon nanotube

In the framework of DM, the equation of motion can be shown in its general form as [54]:

$$\nabla\sigma + F_i = \rho_c \frac{\partial^2 u_i}{\partial t^2} \tag{13}$$

The relation between the macro-stress vector and the micro-stress vector can be expressed in the following form [31]:

$$\{\sigma\} = \{M\}\{p\} \tag{14}$$

Here, $\{M\}$, σ, and p denote the transformation matrix, stress tensor, and strain tensor, respectively, which are defined as follows [31]:

$$\{\sigma\} = \begin{bmatrix} \sigma_{xx} \\ \sigma_{yy} \\ \sigma_{xy} \end{bmatrix}, \{M\} = \begin{bmatrix} (e_{11}^0)^2 & (e_{21}^0)^2 & (e_{31}^0)^2 \\ (e_{12}^0)^2 & (e_{22}^0)^2 & (e_{32}^0)^2 \\ e_{11}^0 e_{12}^0 & e_{21}^0 e_{22}^0 & e_{31}^0 e_{32}^0 \end{bmatrix}, \{p\} = \begin{bmatrix} p_1 \\ p_2 \\ p_3 \end{bmatrix} \tag{15}$$

By taking $k = 1$ in Eq. (9), the equation can be rewritten as [31]:

$$\epsilon_a = e_a^0 (\nabla u) e_a^0 \tag{16}$$

Due to the symmetry illustrated in Fig. 4, Eq. (16) takes the following form:

$$\epsilon_a = \frac{1}{2} e_a^0 \left(\nabla u + \nabla u^T\right) e_a^0 \tag{17}$$

The macro-strain ε is related to the micro-strain ϵ through the following relation [31]:

$$\{\epsilon\} = \left\{M^T\right\}\{\varepsilon\} \tag{18}$$

where,

$$\{\varepsilon\} = \begin{bmatrix} \varepsilon_{xx} \\ \varepsilon_{yy} \\ \varepsilon_{xy} \end{bmatrix}, \{\epsilon\} = \begin{bmatrix} \epsilon_1 \\ \epsilon_2 \\ \epsilon_3 \end{bmatrix} \tag{19}$$

Within classical elasticity theory, the relationship between stress and strain can be expressed as:

$$\{\sigma\} = \{D\}\{\varepsilon\} \tag{20}$$

The rigidity matrix D is defined as follows:

$$\{D\} = \begin{bmatrix} 4G\left(\frac{\Lambda+G}{\Lambda+2G}\right) & \frac{2\Lambda G}{\Lambda+2G} & 0 \\ \frac{2\Lambda G}{\Lambda+2G} & 4G\left(\frac{\Lambda+G}{\Lambda+2G}\right) & 0 \\ 0 & 0 & G \end{bmatrix} \tag{21}$$

Combining Eqs. (14), (18), and (20), we obtain:

$$\{D\} = \{M\}\{A\}\left\{M^T\right\} \tag{22}$$

Here, $\{A\}$ denotes the micro-module matrix, which is defined as follows [31]:

$$\{A\} = \begin{bmatrix} \frac{4G}{9}\left(\frac{7L+10G}{\Lambda+2G}\right) & \frac{4G}{9}\left(\frac{\Lambda-2G}{\Lambda+2G}\right) & \frac{4G}{9}\left(\frac{\Lambda-2G}{\Lambda+2G}\right) \\ \frac{4G}{9}\left(\frac{\Lambda-2G}{\Lambda+2G}\right) & \frac{4G}{9}\left(\frac{7\Lambda+10G}{\Lambda+2G}\right) & \frac{4G}{9}\left(\frac{\Lambda-2G}{\Lambda+2G}\right) \\ \frac{4G}{9}\left(\frac{\Lambda-2G}{\Lambda+2G}\right) & \frac{4G}{9}\left(\frac{\Lambda-2G}{\Lambda+2G}\right) & \frac{4G}{9}\left(\frac{7\Lambda+10G}{\Lambda+2G}\right) \end{bmatrix} \tag{23}$$

Here, Λ and G represent the Lamé constants, which can be expressed in terms of conventional engineering material properties as:

$$\Lambda = \frac{E_c \upsilon}{(1+\upsilon)(1-2\upsilon)} \tag{24}$$

$$G = \frac{E_c}{2(1+\upsilon)} \tag{25}$$

Here, υ is Poisson's ratio. For the plane stress condition, $\Lambda = 2G$ is substituted into Eq. (23), leading to diagonal terms of the form $A_0 = 8\Phi/3 = G$, while the remaining components vanish. In the isotropic case, the matrix M is then constructed as follows [31]:

$$\{M\} = \begin{bmatrix} \cos^2\theta & \cos^2(\theta+60) & \cos^2(\theta+120) \\ \sin^2\theta & \sin^2(\theta+60) & \sin^2(\theta+120) \\ \sin\theta\cos\theta & \sin(\theta+60)\cos(\theta+60) & \sin(\theta+120)\cos(\theta+120) \end{bmatrix} \tag{26}$$

As illustrated in Fig. 4, when the direction vectors are defined as $e_1(1,0,0)$, $e_2(-1/2, \sqrt{3}/2,0)$, $e_3(-1/2, -\sqrt{3}/2,0)$, Eq. (26) can be rewritten in the following form:

$$\{M\} = \begin{bmatrix} 1 & 1/4 & 1/4 \\ 0 & 3/4 & 3/4 \\ 0 & -\sqrt{3}/4 & \sqrt{3}/4 \end{bmatrix} \tag{27}$$

In this study, the Taylor series expansion is truncated to the first three terms; accordingly, the trinomial micro-stresses are obtained from Eq. (9) as follows [31, 54]:

$$\epsilon_a = e_a^0(\nabla u)e_a^0 + \frac{\mu_a}{2}\left[e_a^0\left(e_a^0\nabla\right)\left(e_a^0\nabla u\right)\right] + \frac{\mu_a^2}{6}\left[e_a^0\left(e_a^0\nabla\right)\left(e_a^0\nabla\right)\left(e_a^0\nabla u\right)\right] \tag{28}$$

By expressing e_a^0 within the framework of classical continuum mechanics and adopting the Cartesian representation $\left(\nabla = \frac{\partial}{\partial x_i} t_j\right)$, the previous relation can be rewritten as:

$$\epsilon_a = e_{am}^0 e_{an}^0 \left(\varepsilon_{mn} + \frac{\mu_a}{2} e_{as}^0 \frac{\partial \varepsilon_{mn}}{\partial x_s} + \frac{\mu_a^2}{6} e_{at}^0 e_{as}^0 \frac{\partial^2 \varepsilon_{mn}}{\partial x_t \partial x_s}\right) \tag{29}$$

The macro-stress tensor σ_{ij} takes the following form [31, 54]:

$$\sigma_{ij} = \sum_{a=1}^{d} A_0 e_{ai}^0 e_{aj}^0 e_{am}^0 e_{an}^0 \left(\varepsilon_{mn} + \frac{\mu_a^2}{12} e_{at}^0 e_{as}^0 \frac{\partial^2 \varepsilon_{mn}}{\partial x_t \partial x_s}\right) \tag{30}$$

Under axial loading, the only non-zero stress component is σ_{ij}, which leads to the following equation of motion:

$$\frac{\partial \sigma_{xx}}{\partial x} = \rho_c \frac{\partial^2 u}{\partial t^2} \tag{31}$$

By introducing the stress expressions into the formulation, the governing differential equation for the axial vibration of the nanotube is obtained [54]:

$$A_0 \frac{\partial^2 u}{\partial x^2} + \frac{\mu^2}{12} A_0 \frac{\partial^4 u}{\partial x^4} = \rho_c \frac{\partial^2 u}{\partial t^2} \tag{32}$$

Here, $\mu^2/12$ represents the characteristic microstructural length scale of the material for zigzag nanotube model. When $\mu = 0$, the classical (local) equation is recovered. For nonzero μ, the microstructure influences the dynamic response through the higher-order gradient term. It also should be noted that if we change the chiral angle of the nanotube, the length scale parameter can take different

values, allowing the model to capture various chirality-dependent size effects. The previously derived equation of motion for axial vibration can be reformulated to describe torsional vibration as follows [12, 54]:

$$GJ\frac{\partial^2\phi}{\partial x^2}+\frac{\mu^2}{12}GJ\frac{\partial^4\phi}{\partial x^4}+\rho_c J\frac{\partial^2\phi}{\partial t^2}=0 \tag{33}$$

In this formulation, ϕ denotes the rotation function, while G and J correspond to the shear modulus of composite and polar moment of inertia. Incorporating the Kelvin–Voigt viscoelastic model into the governing equation leads to the following form:

$$\frac{\mu^2}{12}\left(1+c\frac{\partial}{\partial t}\right)GJ\frac{\partial^4\phi}{\partial x^4}+\left(1+c\frac{\partial}{\partial t}\right)GJ\frac{\partial^2\phi}{\partial x^2}+\rho_c J\frac{\partial^2\phi}{\partial t^2}=0 \tag{34}$$

In this context,c represents the viscous damping parameter. In the Kelvin–Voigt viscoelastic model, c corresponds to the retardation time (or delay time). It physically defines the time delay in the material's response to an applied force or deformation. However, this model and parameter are considered a quantity representing the system's energy dissipation in dynamic analyses.

4 Eigenvalue formulation of SFRC nanotubes with deformable boundaries

This section outlines a semi-analytical framework developed to solve the governing equations of SFRC nanotubes. The proposed solution strategy relies on the combined use of Fourier sine series and Stokes' transformation, enabling a unified and efficient treatment of various BCs without requiring case-specific reformulations. As a first step, the rotation function is represented by assuming a harmonic time dependence, such that $\phi(x,\,t)=\aleph(x)e^{i\omega t}$, where ω denotes the angular frequency. Following this representation, the governing equation of motion can be reformulated in terms of the spatial function as:

$$\Omega_1\frac{d^4\aleph}{dx^4}+\Omega_2\frac{d^2\aleph}{dx^2}+\Omega_3\aleph=0 \tag{35}$$

where,

$$\Omega_1=\frac{\mu^2}{12}(1+i\omega c)GJ \tag{36}$$

$$\Omega_2=(1+i\omega c)GJ \tag{37}$$

$$\Omega_3=\omega^2\rho_c J \tag{38}$$

The rotation function is approximated by a Fourier sine series, which ensures a consistent representation over the interior domain $(0<x<L)$ while simultaneously satisfying the conditions at the boundary points $x=0$ and $x=L$, as expressed by [72]:

$$\aleph(x)=\begin{cases}\aleph_0, x=0,\\ \aleph_L, x=L,\\ \sum_{r=1}^{\infty}b_r sin(\beta_r x), 0<x<L\end{cases} \tag{39}$$

Here, $\beta_r=r\pi/L$, and b_r corresponds to the Fourier sine series coefficient, defined as follows:

$$b_r=\frac{2}{L}\int_0^L\aleph(x)sin(\beta_r x)dx \tag{40}$$

Through the application of the Stokes transformation, the derivatives of the rotation function are represented in a Fourier series form. Consequently, the first derivative corresponding to Eq. (39) can be written as:

$$\aleph\prime(x)=\sum_{r=1}^{\infty}\beta_r b_r cos(\beta_r x) \tag{41}$$

The above equation can be further expressed in terms of a Fourier cosine series as:

$$\aleph\prime(x)=\frac{c_0}{2}+\sum_{r=1}^{\infty}c_r cos(\beta_r x) \tag{42}$$

The Fourier series coefficients, c_0 and c_r, are subsequently obtained as:

$$c_0=\frac{2}{L}\int_0^L\aleph\prime(x)dx=\frac{2}{L}(\aleph_L-\aleph_0) \tag{43}$$

$$c_r = \frac{2}{L}\int_0^L \aleph\prime(x)cos(\beta_r x)dx, (r = 1,2, \dots) \tag{44}$$

By performing integration by parts, the coefficient c_r can be expressed as:

$$c_r = \frac{2}{L}[\aleph(x)cos(\beta_r x)]_0^L + \frac{2}{L}\left[\beta_r \int_0^L \aleph(x)sin(\beta_r x)dx\right] = \frac{2(-1)^r(\aleph_L - \aleph_0)}{L} + \beta_r b_r \tag{45}$$

By applying Stokes' transformations, the first four derivatives of ℵ(x) are systematically expressed in the form presented in [72]:

$$\aleph\prime(x) = \frac{(\aleph_L - \aleph_0)}{L} + \sum_{r=1}^{\infty} cos(\beta_r x)\left(\frac{2\left[(-1)^r\aleph_L - \aleph_0\right]}{L} + \beta_r b_r\right) \tag{46}$$

$$\aleph''(x) = -\sum_{r=1}^{\infty} \beta_r sin(\beta_r x)\left(\frac{2\left[(-1)^r\aleph_L - \aleph_0\right]}{L} + \beta_r b_r\right) \tag{47}$$

$$\aleph'''(x) = \frac{\aleph_L'' - \aleph_0''}{L} + \sum_{r=1}^{\infty} cos(\beta_r x)\left[\frac{2\left[\aleph_L''(-1)^r - \aleph_0''\right]}{L} - {\beta_r}^2\left(\frac{2\left[(-1)^r\aleph_L - \aleph_0\right]}{L} + \beta_r b_r\right)\right] \tag{48}$$

$$\aleph^{(4)}(x) = -\sum_{r=1}^{\infty} \beta_r sin(\beta_r x)\left[\frac{2\left[\aleph_L''(-1)^r - \aleph_0''\right]}{L} - {\beta_r}^2\left(\frac{2\left[(-1)^r\aleph_L - \aleph_0\right]}{L} + \beta_r b_r\right)\right] \tag{49}$$

Upon inserting Eqs. (39), (47), and (49) into Eq. (35), the coefficient b_r can be expressed as:

$$b_r = \frac{2\beta_r(-\Omega_2 + \Omega_1{\beta_r}^2)(\aleph_0 + (-1)^{1+r}\aleph_L)}{L(\Omega_3 - \Omega_2{\beta_r}^2 + \Omega_1{\beta_r}^4)} \tag{50}$$

The force BCs at the deformable ends are formulated as:

$$x = 0 \rightarrow -\Omega_1\frac{\partial^3\phi}{\partial x^3} - \Omega_2\frac{\partial\phi}{\partial x} = \Omega\phi \tag{51}$$

$$x = L \rightarrow -\Omega_1\frac{\partial^3\phi}{\partial x^3} - \Omega_2\frac{\partial\phi}{\partial x} = -\Omega\phi \tag{52}$$

$$-\Omega_1\frac{d^3\aleph}{dx^3} - \Omega_2\frac{d\aleph}{dx}|_{x=0} = \psi_0\aleph_0 \tag{53}$$

$$-\Omega_1\frac{d^3\aleph}{dx^3} - \Omega_2\frac{d\aleph}{dx}|_{x=L} = -\psi_L\aleph_L \tag{54}$$

Here, ψ_0 and ψ_L represent the torsional spring stiffnesses at the beam ends. Very high values ψ_0 and ψ_L effectively simulate clamped–clamped (C–C) BCs, whereas lower values ψ_L correspond to clamped–free (C–F) boundaries. The resulting eigenvalue problem is then formulated by substituting Eqs. (46), (48), and (50) into Eqs. (53) and (54), yielding:

$$\left(\left(-\psi_0 + \frac{\Omega_2}{L}\right) + \sum_{r=1}^{N}\frac{2L(-r^2\pi^2\Omega_1 + L^2\Omega_2)\Omega_3}{r^4\pi^4\Omega_1 - L^2r^2\pi^2\Omega_2 + L^4\Omega_3}\right)\aleph_0 + \left(-\frac{\Omega_2}{L} + \sum_{r=1}^{N}\frac{2(-1)^r L(r^2\pi^2\Omega_1 - L^2\Omega_2)\Omega_3}{r^4\pi^4\Omega_1 - L^2r^2\pi^2\Omega_2 + L^4\Omega_3}\right)\aleph_L = 0 \tag{55}$$

$$\left(-\frac{\Omega_2}{L} + \sum_{r=1}^{N}\frac{2(-1)^r L(r^2\pi^2\Omega_1 - L^2\Omega_2)\Omega_3}{r^4\pi^4\Omega_1 - L^2r^2\pi^2\Omega_2 + L^4\Omega_3}\right)\aleph_0 + \left(\left(-\psi_L + \frac{\Omega_2}{L}\right) + \sum_{r=1}^{N}\frac{2L(-r^2\pi^2\Omega_1 + L^2\Omega_2)\Omega_3}{r^4\pi^4\Omega_1 - L^2r^2\pi^2\Omega_2 + L^4\Omega_3}\right)\aleph_L = 0 \tag{56}$$

Here, N denotes the number of terms used in the series. Although Fourier series theoretically consist of an infinite number of terms, in order to perform a numerical solution, the series must be represented by a finite number of terms and limited to an appropriate value of N.

By accounting for the effects of spring stiffness, material properties, and scale-dependent factors through Eqs. (55) and (56), the resulting eigenvalue problem can be expressed in matrix form as:

$$det\begin{bmatrix}\Pi_{11} & \Pi_{12}\\ \Pi_{21} & \Pi_{22}\end{bmatrix} = 0 \tag{57}$$

where,

$$\Pi_{11} = \left(-\psi_0 + \frac{\Omega_2}{L}\right) + \sum_{r=1}^{N}\frac{2L(-r^2\pi^2\Omega_1 + L^2\Omega_2)\Omega_3}{r^4\pi^4\Omega_1 - L^2r^2\pi^2\Omega_2 + L^4\Omega_3} \tag{58}$$

Table 1 Comparison of torsional NDFs for viscoelastic nanotubes ($\psi_0 = \psi_L = 10^9$ nN.nm/rad, $L = 20$ nm)

η_c	$\mu = 1.0$ nm		$\mu = 3.0$ nm		$\mu = 5.0$ nm	
	Ref. [15]	This study	Ref. [15]	This study	Ref. [15]	This study
0.00	3.138	3.138	3.112	3.112	3.06	3.06
0.01	3.138 + 0.049i	3.138 + 0.049i	3.112 + 0.048i	3.112 + 0.048i	3.059 + 0.047i	3.059 + 0.047i
0.02	3.137 + 0.098i	3.137 + 0.098i	3.111 + 0.097i	3.111 + 0.097i	3.058 + 0.094i	3.058 + 0.094i
0.03	3.135 + 0.148i	3.135 + 0.148i	3.109 + 0.145i	3.109 + 0.145i	3.057 + 0.14i	3.057 + 0.14i
0.04	3.132 + 0.197i	3.132 + 0.197i	3.106 + 0.194i	3.106 + 0.194i	3.054 + 0.187i	3.054 + 0.187i
0.05	3.129 + 0.246i	3.129 + 0.246i	3.103 + 0.242i	3.103 + 0.242i	3.051 + 0.234i	3.051 + 0.234i
0.06	3.124 + 0.295i	3.124 + 0.295i	3.099 + 0.291i	3.099 + 0.291i	3.047 + 0.281i	3.047 + 0.281i
0.07	3.119 + 0.345i	3.119 + 0.345i	3.094 + 0.339i	3.094 + 0.339i	3.042 + 0.328i	3.042 + 0.328i
0.08	3.114 + 0.394i	3.114 + 0.394i	3.088 + 0.387i	3.088 + 0.387i	3.037 + 0.374i	3.037 + 0.374i
0.09	3.107 + 0.443i	3.107 + 0.443i	3.082 + 0.436i	3.082 + 0.436i	3.031 + 0.421i	3.031 + 0.421i
0.10	3.099 + 0.492i	3.099 + 0.492i	3.074 + 0.484i	3.074 + 0.484i	3.024 + 0.468i	3.024 + 0.468i

$$\Pi_{12} = -\frac{\Omega_2}{L} + \sum_{r=1}^{N} \frac{2(-1)^r L\left(r^2\pi^2\Omega_1 - L^2\Omega_2\right)\Omega_3}{r^4\pi^4\Omega_1 - L^2r^2\pi^2\Omega_2 + L^4\Omega_3} \tag{59}$$

$$\Pi_{21} = -\frac{\Omega_2}{L} + \sum_{r=1}^{N} \frac{2(-1)^r L(r^2\pi^2\Omega_1 - L^2\Omega_2)\Omega_3}{r^4\pi^4\Omega_1 - L^2r^2\pi^2\Omega_2 + L^4\Omega_3} \tag{60}$$

$$\Pi_{22} = \left(-\psi_L + \frac{\Omega_2}{L}\right) + \sum_{r=1}^{N} \frac{2L(-r^2\pi^2\Omega_1 + L^2\Omega_2)\Omega_3}{r^4\pi^4\Omega_1 - L^2r^2\pi^2\Omega_2 + L^4\Omega_3} \tag{61}$$

5 Numerical results

This section focuses on the numerical results obtained for the free torsional vibration of SFRC nanobeams, with particular attention given to how key material properties and geometric parameters affect their dynamic behavior. Both the natural frequencies and the viscous damping coefficients are expressed in nondimensional form ($\overline{\omega}$ and η_c, respectively). The definitions of the nondimensional frequency (NDF) and nondimensional viscous damping parameter (NDVDP) are provided as follows:

$$\overline{\omega} = \omega L\sqrt{\frac{\rho_m}{G_m}} \tag{62}$$

$$\eta_c = \frac{c}{L\sqrt{\frac{\rho_m}{G_m}}} \tag{63}$$

The shear modulus of the matrix is given by $G_m = E_m/[2(1+\upsilon)]$ is valid. It should be noted that most of the NDFs presented in this section account for damping effects; consequently, the frequencies generally possess both real ($\overline{\omega}_{Real}$) and imaginary ($\overline{\omega}_{Img}$) components. In the present analysis, extremely high torsional spring stiffnesses ($\psi_0 = \psi_L = 10^9$ nN nm/rad) are used to simulate C–C BCs, while the C–F configuration is modeled by assigning $\psi_0 = 10^9$ nN.nm/rad one end and $\psi_L = 10^{-6}$ nN nm/rad at the other. Unless specified otherwise, the following parameters are kept constant: $E_m = 1$ TPa, $\rho_m = 1.3$ kg/m^3, $E_f/E_m = 100$, $\rho_f/\rho_m = 1.5, l/d = 10$, $V_f = 0.02$, $R = 1$ nm, $L = 10$R nm, $\mu = 1$ nm, $\eta_c = 0.05$, and $\psi_0 = \psi_L = 10^9$ nN nm/rad. Furthermore, since the series used in the solution have an infinite number of terms, it is not practically possible to compute them directly. For this reason, the series expansion in the results obtained has been limited to 1000 terms ($N = 1000$).

First, the proposed approach is validated for the C–C BC by comparing the NDFs of SFRC nanobeams with the closed-form results reported by Kadıoğlu and Yaylı [15], as presented in Table 1. Excellent agreement is observed across different scale parameters, confirming that the method accurately captures size-dependent effects. The solution also performs well when viscous damping is included, demonstrating that both material and NDVDPs are effectively incorporated within the Fourier sine series framework. Notably, this high level of accuracy can be achieved using a relatively low number of terms in the series expansion, thanks to the rapid convergence properties of the sine series for the considered boundary configuration.

Table 2 compares the fundamental torsional NDFs predicted by the present DM model and the nonlocal elasticity model reported by Akpınar et al. [60] for SFRC nanobeams. For the classical case (scale parameter = 0), both models yield almost identical results, with a negligible difference of approximately 0.18%. This small discrepancy arises from the calculation of the shear modulus;

Table 2 Comparison of torsional NDFs of SFRC nanobeams (C–C) predicted by DM and nonlocal elasticity [60] for different scale parameters, nanotube lengths, and fiber aspect ratios

L (nm)	l/d	Nonlocal elasticity [60] ($\eta = 0$ nm)	DM ($\mu = 0$ nm)	Nonlocal elasticity [60] ($\eta = 1$ nm)	DM ($\mu = 1$ nm)	Nonlocal elasticity [60] ($\eta = 3$ nm)	DM ($\mu = 3$ nm)
10	10	3.2729	3.2671	3.1225	3.2537	2.3818	3.1439
	20	3.2792	3.2727	3.1284	3.2592	2.3864	3.1492
	30	3.2814	3.2747	3.1306	3.2612	2.3880	3.1512
20	10	3.2729	3.2671	3.2333	3.2638	2.9607	3.2367
	20	3.2792	3.2727	3.2395	3.2693	2.9663	3.2423
	30	3.2814	3.2747	3.2417	3.2713	2.9684	3.2443

reference [60] uses $G_c = E_c/[2(1+\upsilon_c)]$ as given, while the present study follows the same relation consistently. Notably, the percentage increases in torsional NDFs due to increasing the fiber aspect ratio (l/d) remain identical for both theories and across all scale parameter values. This is because the Halpin–Tsai model governs the elastic properties, and both theories share the same underlying material property inputs. When the scale parameter increases from 0 to 3 nm, the two theories diverge significantly. Nonlocal elasticity predicts a pronounced softening (up to 27% reduction at $L = 10$ nm), whereas DM predicts a much milder size-dependent response (approximately 4% reduction under the same conditions). This difference stems from the distinct mathematical foundations of the two theories: nonlocal elasticity employs an integral-type constitutive relation, while DM is a higher-grade continuum theory based on microstructural doublet interactions.

Figure 5a–d show how the NDVDP affects the torsional NDFs of SFRC nanotubes. The plots correspond to the first four torsional modes: Fig. 5a is mode 1, Fig. 5b mode 2, Fig. 5c mode 3, and Fig. 5d mode 4. Two BCs, C–C and C–F, are compared in each case. As NDVDP increases from 0.01 to 0.1, the real parts of the NDFs change as follows: for mode 1, the decrease is about 1.4% for C–C and 0.3% for C–F; for mode 2, the decrease is roughly 5.4% for C–C and 3% for C–F; for mode 3, the decrease reaches around 12% for C–C and 8.5% for C–F; and for mode 4, the reduction is about 21% for C–C and 16.4% for C–F. In general, real NDFs decrease more noticeably for higher modes, while frequencies under C–F are slightly lower than under C–C. Systems with more rigid BCs, like C–C, dissipate energy more efficiently. As a result, the real part of the frequency decreases faster with increasing damping. In contrast, under less rigid conditions, such as C–F, the frequency decreases more slowly.

Figure 6a–d show the influence of the NDVDP on the torsional NDFs of SFRC nanotubes over a wider damping range, up to 0.25. Unlike the more regular behavior seen in Fig. 5 at maximum of 10% damping, here some unexpected trends emerge. In mode 1 (Fig. 6a), the real parts of the NDFs show a consistent decrease of about 9% as NDVDP increases from 0.025 to 0.25. Increasing the scale parameter in DM theory reduces the NDFs, indicating a weakening effect. Increasing the scale parameter results in frequency changes of approximately − 1.6% at $\eta_c = 0.025$ and about − 1.3% at $\eta_c = 0.25$, indicating a relatively stable influence without any reversal. For mode 2 (Fig. 6b), at an NDVDP value of 0.225, the effect of the scale parameter on frequencies changes noticeably. Similarly, in mode 3 (Fig. 6c), this inversion occurs around $\eta_c = 0.175$, while for mode 4 (Fig. 6d), at $\eta_c = 0.125$, increasing the scale parameter ceases to strengthen the NDFs and may even reverse its effect. These observations suggest that the damping effect varies significantly with mode number, with higher modes experiencing stronger damping and NDFs approaching zero. Quantitatively, the real parts of the NDFs decrease by approximately 9% in mode 1 and 44% in mode 2 as damping increases from 0.025 to 0.25. In modes 3 and 4, the NDFs are fully damped at specific NDVDP values—mode 3 at $\eta_c = 0.2008$ (for $\mu = 0$ nm) and mode 4 at $\eta_c = 0.1506$ (for $\mu = 0$ nm)— resulting in the complete disappearance of torsional vibrations. This may be one of the fundamental limitations of the Kelvin-Voigt model. In this context given the potential for such nonlinear and unexpected behavior at higher damping levels, an NDVDP value of 0.05 (5%) has been chosen for the subsequent parts of this study to avoid numerical anomalies and maintain consistent results.

Figure 7a–d present the variation of the first four torsional NDFs of the SFRC nanotube with respect to the E_f/E_m ratio and the NDVDP. Overall, increasing E_f/E_m from 10 to 100 causes a nearly uniform and modest increase in NDFs of about 3.9% across all modes under zero damping. However, this effect weakens with increasing damping, dropping to approximately 3.75%, 3.4%, 2.75%, and 1.6% for $\eta_c = 0.1$ in the first through fourth modes, respectively. Moreover, increasing NDVDP from 0 to 0.1 reduces the NDFs by approximately − 1.3% in the first mode, − 5% in the second mode, − 11.3% in the third mode, and − 19.7% in the fourth mode at $E_f/E_m = 10$, with even slightly larger reductions at higher stiffness ratios (reaching about − 1.4%, − 5.5%, − 12.2%, and − 21.4%, respectively, at $E_f/E_m = 100$). These results suggest that higher vibration modes are much more sensitive to damping effects, whereas the increase in stiffness associated with higher E_f/E_m ratios leads to a relatively uniform and modest change. From a physical point of view, increasing the fiber stiffness primarily improves the overall rigidity of the structure. In contrast, damping mechanisms act by dissipating vibrational energy, and their influence becomes more pronounced in higher-order modes, where the deformation patterns are more complex.

Figure 8a–d illustrates the variation of the first four torsional NDFs of the SFRC nanotube with respect to the mass density ratio ρ_f/ρ_m and the NDVDP. Overall, increasing ρ_f/ρ_m from 1.1 to 2 leads to a consistent but slight decrease in NDFs across

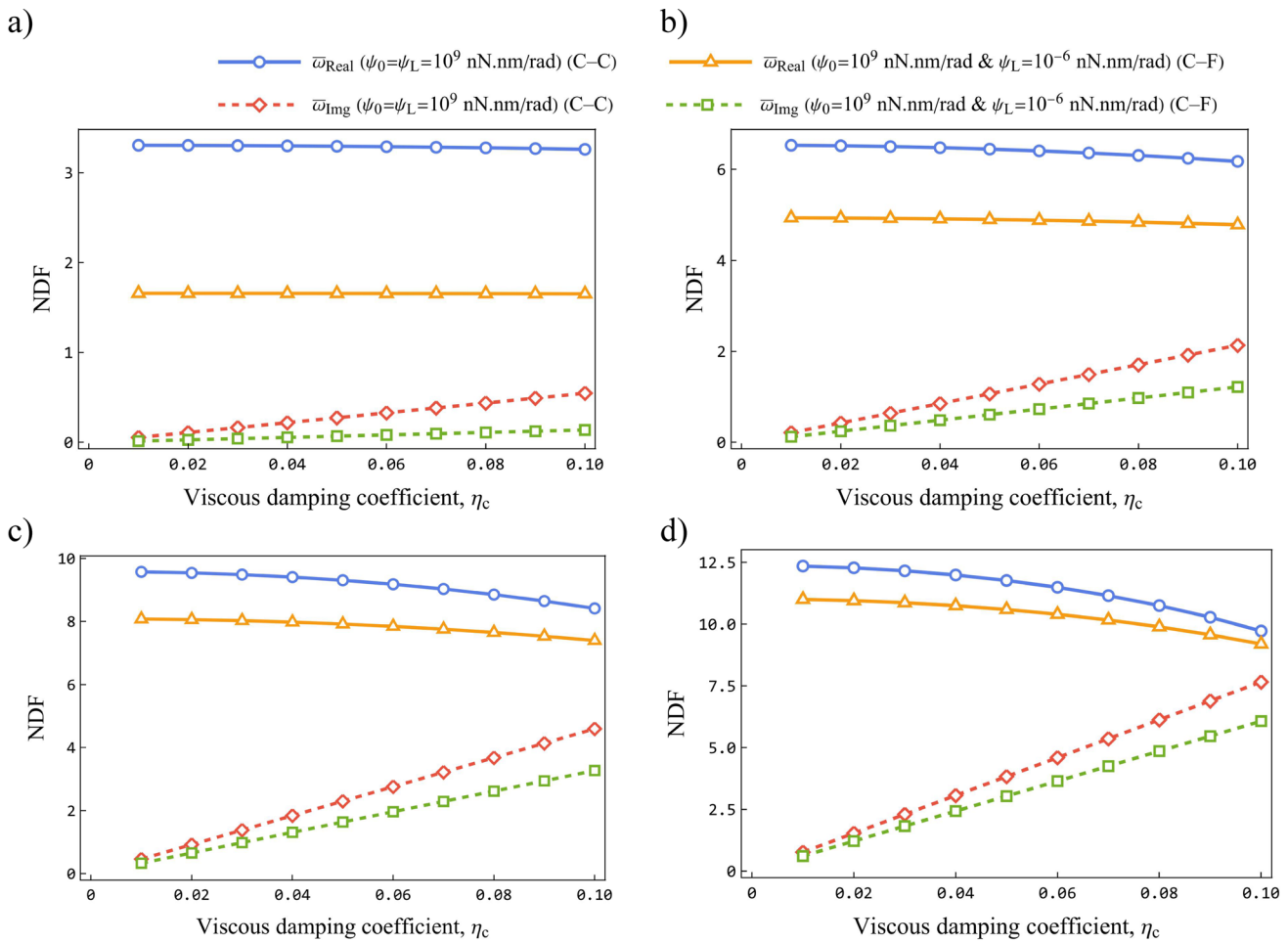


Fig. 5 Comparison of torsional NDFs for SFRC nanotubes under C–C and C–F BCs at different NDVDPs: **a** Mode 1, **b** Mode 2, **c** Mode 3, **d** Mode 4

all modes, with nearly identical reductions of about − 0.88% under zero damping. This decrease remains nearly uniform for all damping values, indicating that the mass density ratio primarily governs this trend rather than damping. For example, the NDFs drop by approximately − 0.86% to − 0.89% in the first mode, − 0.78% to − 0.89% in the second mode, − 0.62% to − 0.88% in the third mode, and − 0.34% to − 0.88% in the fourth mode as ρ_f/ρ_m increases from 1.1 to 2 across all damping levels. This indicates that while increasing fiber mass slightly lowers the system's natural frequencies, damping remains the dominant factor, especially in higher modes. Physically, this trend can be attributed to the increase in inertia with higher fiber density, which reduces vibrational frequencies.

Figure 9a–d shows the effects of fiber volume fraction (V_f) and the NDVDP on the first four torsional NDFs of SFRC nanotubes. Increasing V_f from 0.005 to 0.05 causes a significant and consistent increase in NDFs across all modes, with percentage rises around 14.8% under zero damping. This positive trend remains stable in first mode across all damping levels, indicating that the fiber volume fraction primarily controls the increase in frequencies rather than damping effects. However, in higher modes, the influence of fiber volume fraction becomes less dominant as damping increases, causing the percentage increase in NDFs to gradually diminish. For instance, the NDFs increase by approximately 12.96% to 14.94% in the second mode, 9.99% to 14.94% in the third mode, and 4.71% to 14.94% in the fourth mode as V_f varies from 0.005 to 0.05 at different damping values. The results show that increasing the fiber volume fraction leads to higher torsional stiffness and, consequently, higher natural frequencies. However, damping has a pronounced reducing effect on these frequencies, particularly in the higher modes. This behavior can be understood by considering that a greater fiber content mainly improves the overall rigidity of the composite. In contrast, damping mechanisms may dissipate vibrational energy more effectively in higher-order modes, where the deformation patterns are more complex.

Figure 10a–d illustrates the variation of the first four torsional NDFs of the SFRC nanotube with respect to the fiber aspect ratio (l/d) and NDVDP. Overall, increasing the NDVDP from 0.0 to 0.1 leads to a consistent reduction in NDFs across all modes, with the magnitude of reduction becoming more pronounced for higher modes. In contrast, increasing the *l/d* from 10 to 20 results in a gradual increase in NDFs; for undamped case, this increase is nearly identical across all modes (≈3.34%), indicating a uniform stiffening effect due to geometric slenderness. However, as the η_c increases, this trend becomes mode-dependent, and the percentage

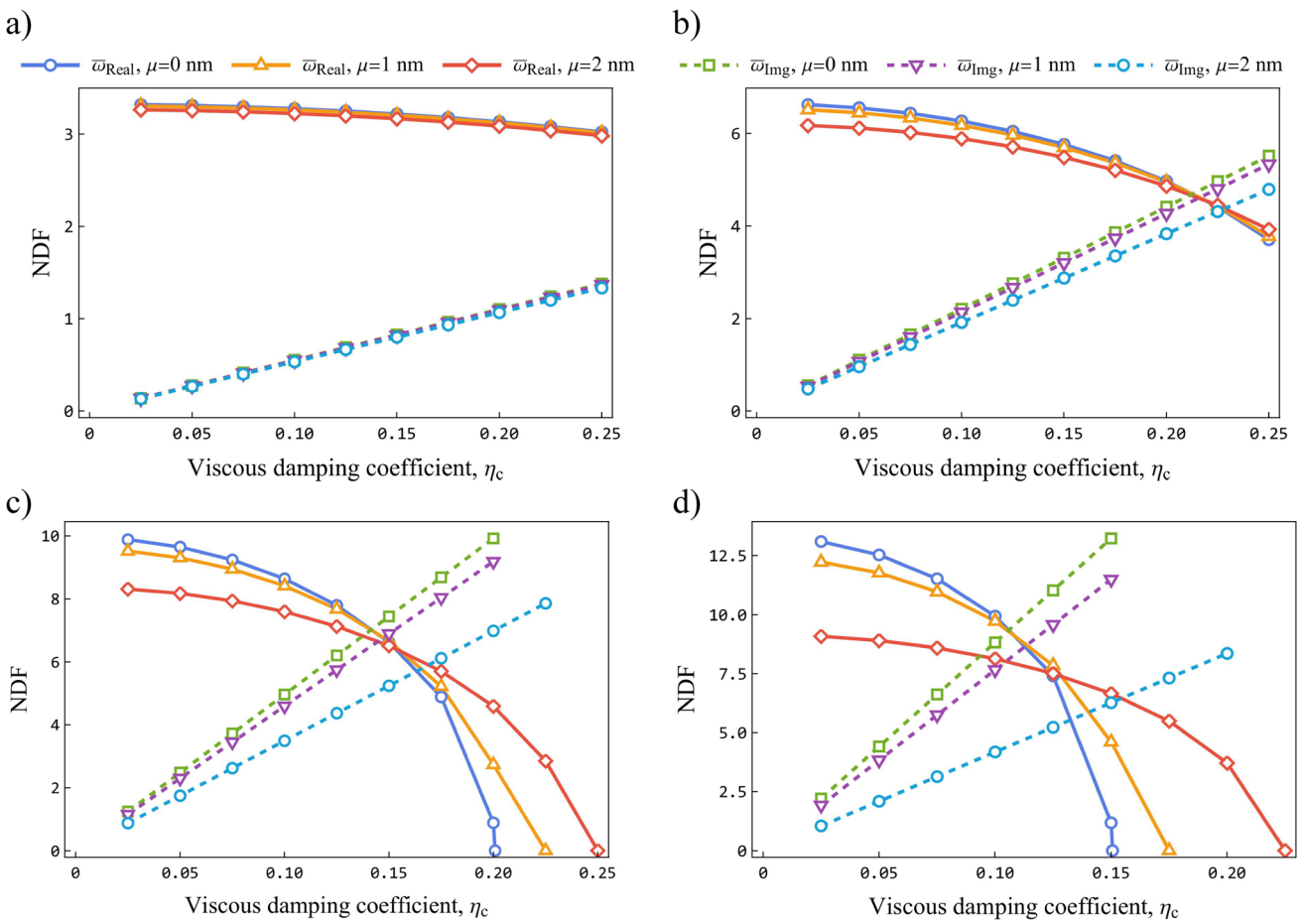


Fig. 6 Comparison of torsional NDFs for SFRC nanotubes at higher NDVDPs and varying scale parameters: **a** Mode 1, **b** Mode 2, **c** Mode 3, **d** Mode 4

changes start to diverge; for instance, at $\eta_c = 0.1$, the increase is about 3.24% for the first mode, while it decreases to approximately 2.92%, 2.29%, and 1.14% for the second, third, and fourth modes, respectively, clearly showing that higher damping reduces the sensitivity of higher modes to aspect ratio variations. These results suggest that damping has a mode-dependent softening effect, while an increase in the aspect ratio increases stiffness and, consequently, the torsional response of the SFRC nanotube.

Figure 11a–d presents the variation of the first four torsional NDFs of the SFRC nanotube with respect to the nanotube length (L) under different scale parameters. It is clearly observed that for the classical case ($\mu = 0.0$), the NDFs remain constant with increasing length, whereas introducing size-dependent effects ($\mu = 1.0$ nm and $\mu = 2.0$ nm) leads to a length-dependent response. Specifically, increasing the μ from 0 to 2 nm results in a noticeable reduction in NDFs, and this reduction is significantly more pronounced at smaller lengths. For example, at $L = 10$ nm, the decreases reach approximately − 1.6%, − 6.6%, − 15.3%, and − 29% for the first through fourth modes, respectively. At $L = 50$ nm these reductions diminish to about − 0.07%, − 0.26%, − 0.56%, and − 0.93%. On the other hand, increasing the nanotube length from 10 to 50 leads to an increase in NDFs for nonzero scale parameters, with percentage increases becoming more significant at higher scale parameters and higher modes; for instance, at $\mu = 1.0$ nm, the increases are about 0.39%, 1.57%, 3.52%, and 6.20%, whereas at $\mu = 2.0$ nm, they rise markedly to approximately 1.61%, 6.84%, 17.39%, and 39.48% for the first to fourth modes, respectively. These findings indicate that size-dependent effects induce a softening behavior that is dominant at smaller length scales and higher modes, while increasing length mitigates this effect.

Overall, the results demonstrate that the proposed model provides an accurate and efficient way to predict the torsional response of SFRC nanostructures, while also accounting for size-dependent effects. Among the parameters considered, NDVDP stands out as the most influential one, particularly in higher modes, where it can lead to a significant reduction in NDFs and, at sufficiently high levels, may even suppress the vibration response. By comparison, material and geometric parameters—such as stiffness ratio, mass density, fiber volume fraction, aspect ratio, and length—have a more moderate impact. Their influence is mainly associated with variations in stiffness and inertia. In contrast, scale effects may become increasingly important at smaller length scales and in higher modes, where they introduce a noticeable softening in the overall behavior.

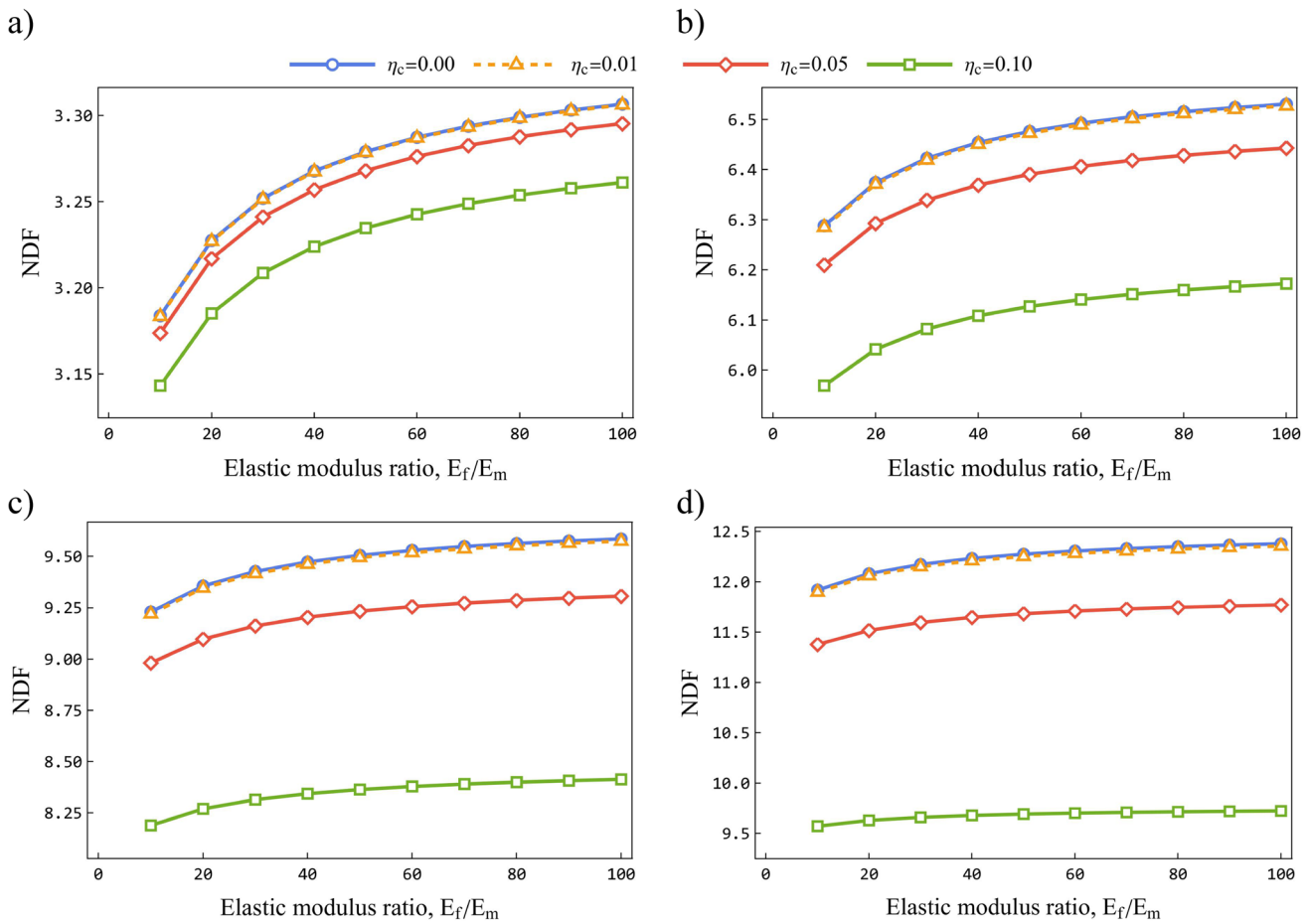


Fig. 7 Torsional frequency response of SFRC nanotubes under varying E_f/E_m ratios and NDVDP levels: **a** First mode, **b** Second mode, **c** Third mode, **d** Fourth mode

6 Conclusions

This study has conducted a detailed analysis of torsional vibrations in SFRC nanotubes, incorporating DM theory to capture size-dependent effects, Kelvin–Voigt viscoelasticity for damping, and torsional spring BCs for more realistic support modeling. The effective properties of the fiber-reinforced composite were determined using the Halpin–Tsai model. A generalized semi-analytical solution was developed using a Fourier sine series expansion, with Stokes' transformation applied to ensure that the physical BCs at the elastic torsional springs are satisfied. A key advantage of this unified approach is its flexibility: any combination of BCs—from fully clamped (infinite spring stiffness) to completely free (zero spring stiffness)—can be handled simply by adjusting the spring parameters, without needing to reformulate the solution framework. The numerical results highlight several important observations:

- The proposed method aligns very well with existing closed-form solutions, demonstrating accuracy even when only a few terms are used in the Fourier series.
- Damping has a significant effect on torsional natural frequencies, particularly for higher modes, which can be strongly suppressed at high damping levels.
- Material parameters influence the frequencies in opposite ways: increasing the fiber-to-matrix stiffness ratio (E_f/E_m) raises the natural frequencies, while a higher mass density ratio (ρ_f/ρ_m) tends to lower them.
- Increasing the fiber volume fraction generally raises frequencies, especially in lower modes, while damping increasingly affects higher modes.
- Larger fiber aspect ratios (l/d) enhance torsional stiffness, although higher modes become less sensitive to geometric changes when damping is considered.
- Nanotube length mainly affects natural frequencies under size-dependent effects, with shorter tubes exhibiting more pronounced softening due to size-dependent effects.
- Scale parameters introduce softening that depends on both the mode and the length, with stronger effects appearing in higher modes.

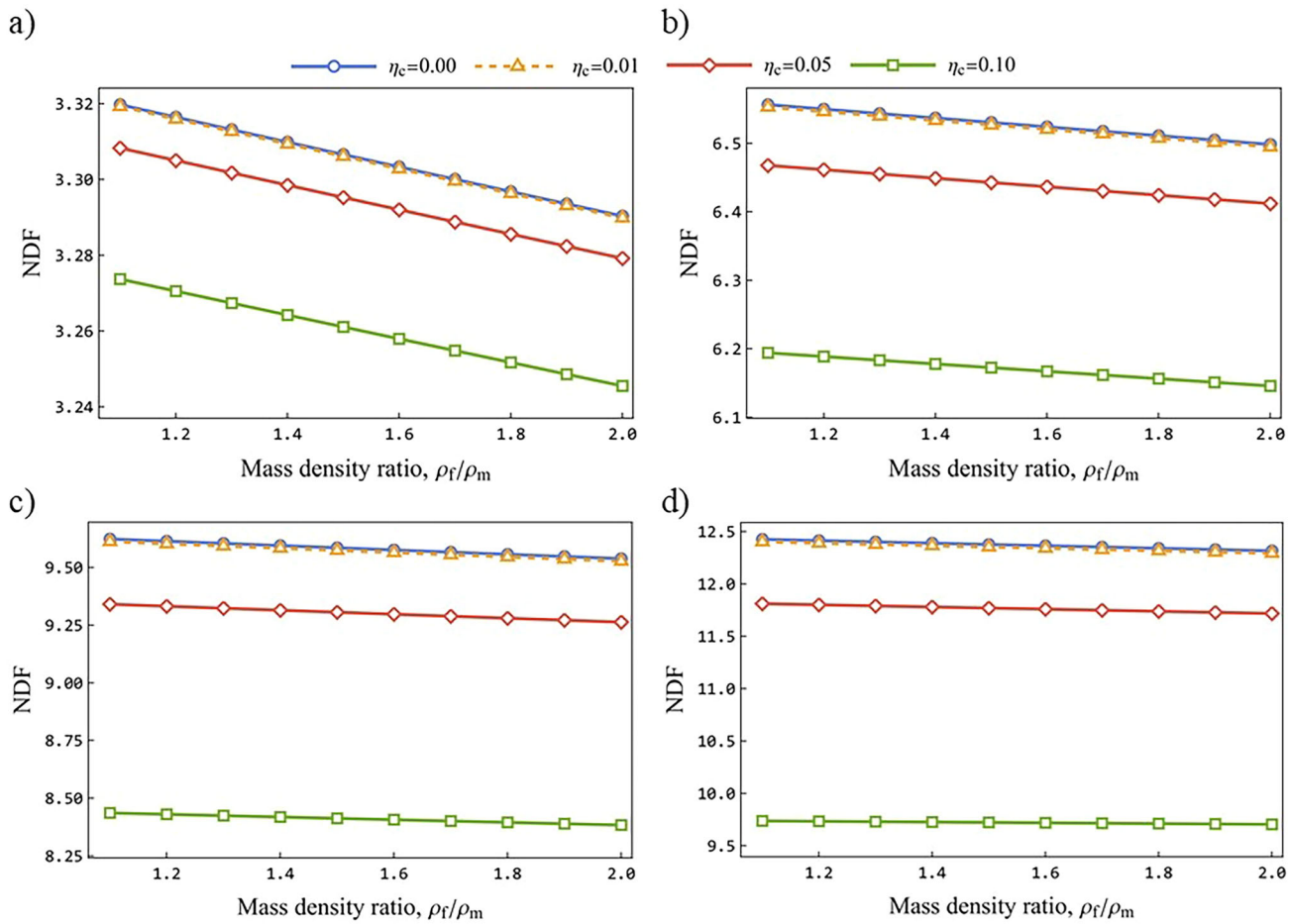


Fig. 8 Variation of torsional NDFs with mass density ratio and NDVDP in SFRC nanotubes: **a** Mode 1, **b** Mode 2, **c** Mode 3, **d** Mode 4

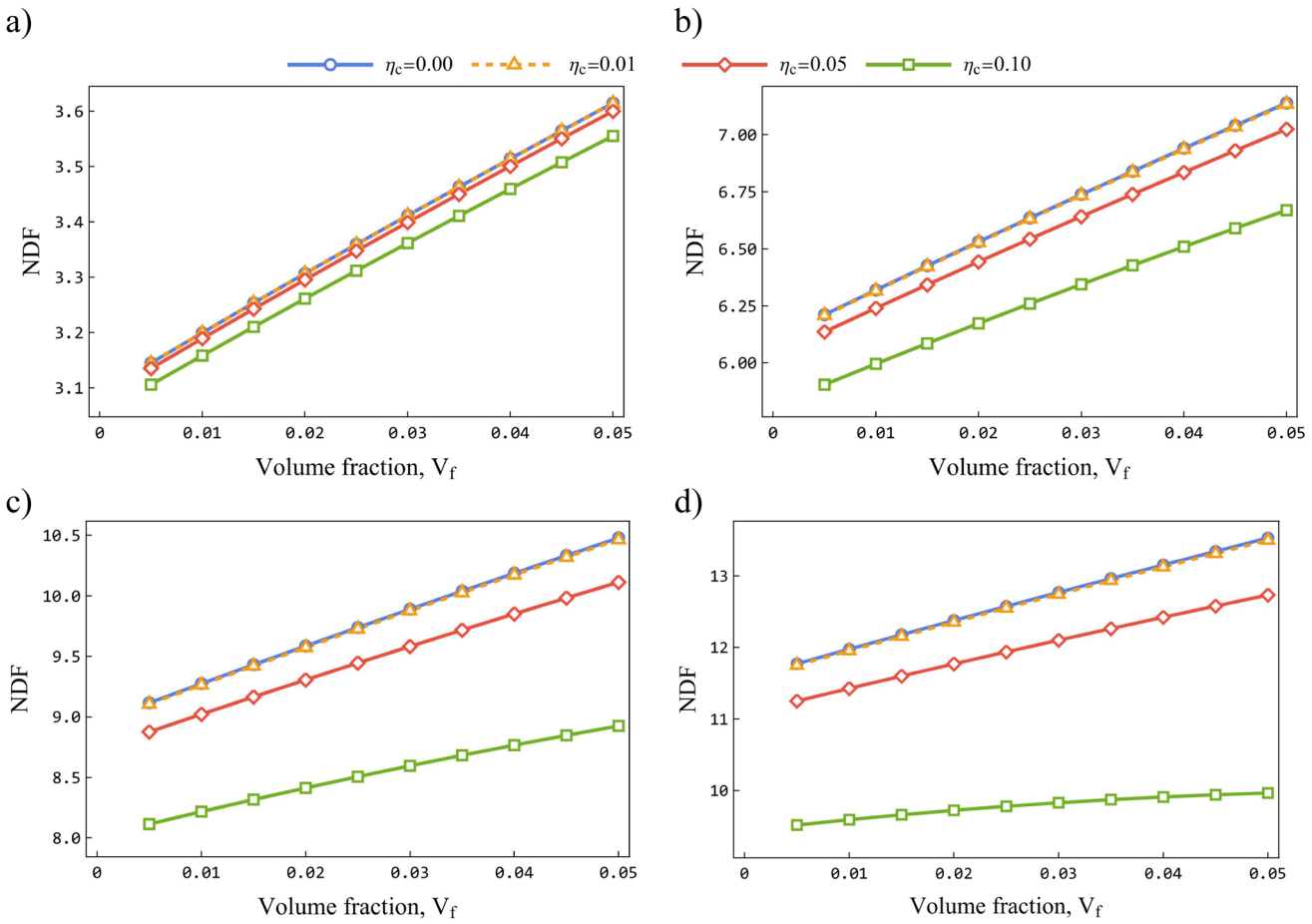


Fig. 9 Variation of torsional NDFs with fiber fraction and NDVDP: **a** First mode, **b** Second mode, **c** Third mode, **d** Fourth mode

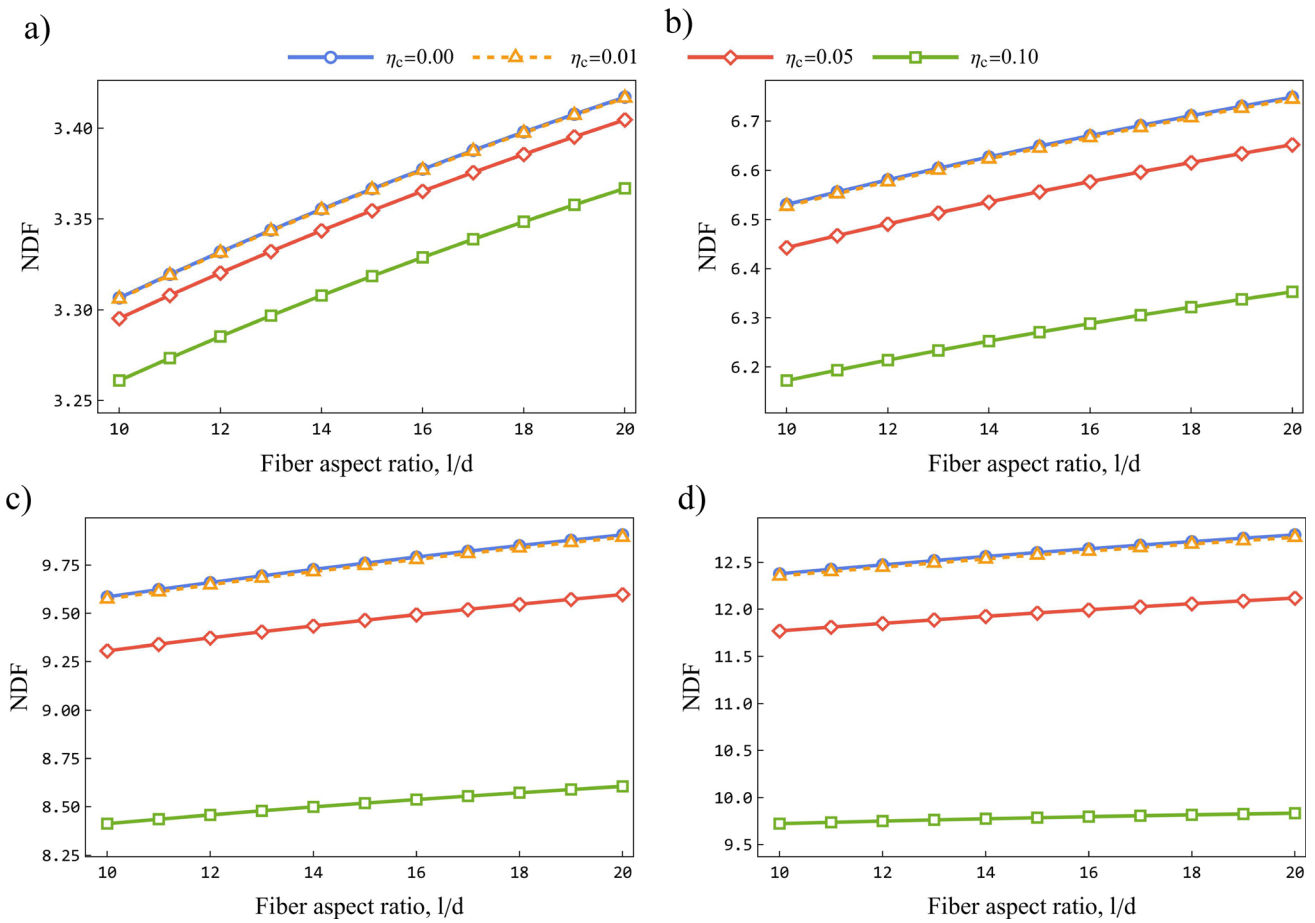


Fig. 10 Effect of aspect ratio on torsional NDFs of SFRC nanotubes for different NDVDPs: **a** Mode 1, **b** Mode 2, **c** Mode 3, and **d** Mode 4

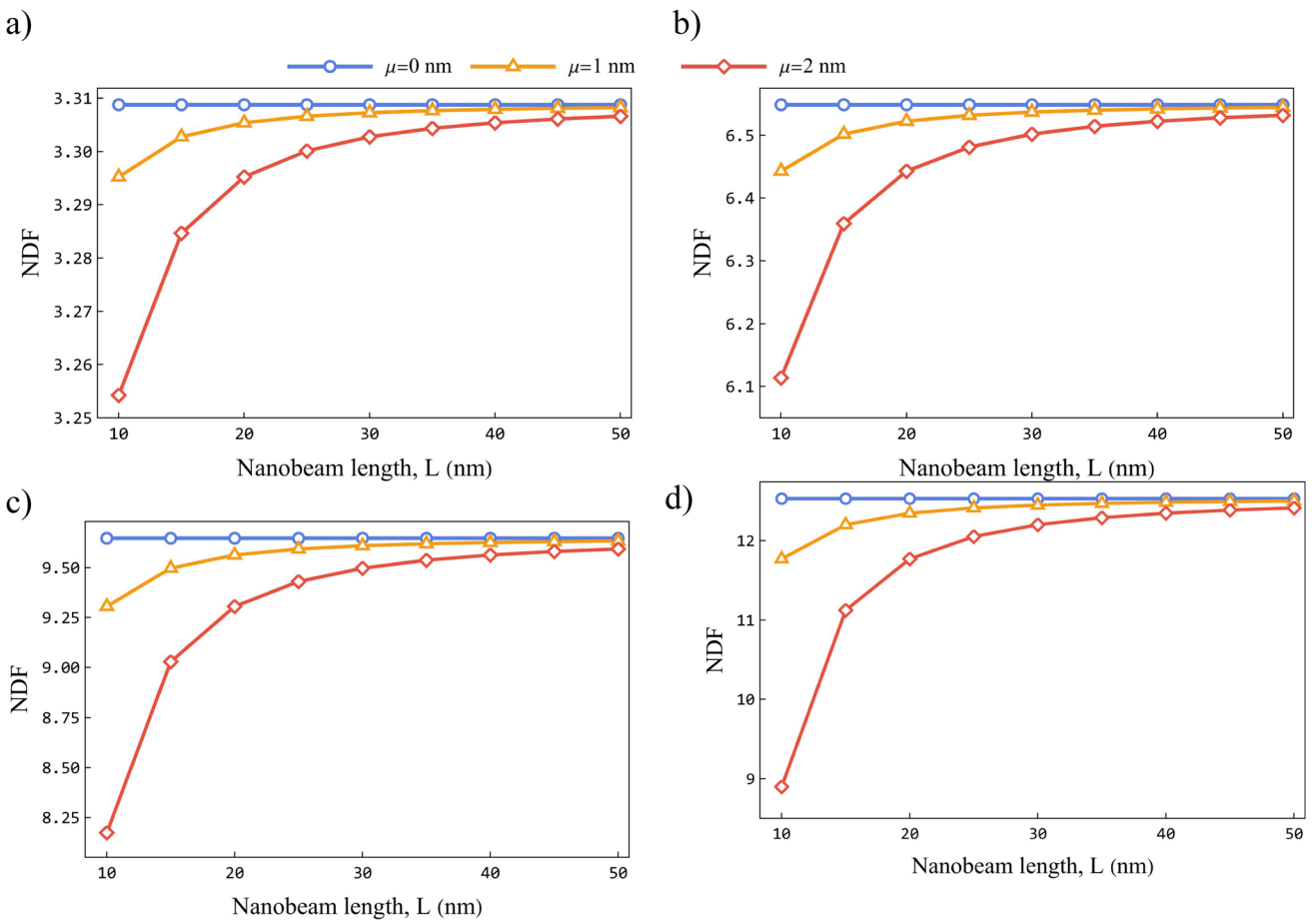


Fig. 11 Influence of scale parameter on torsional NDFs of SFRC nanotubes at various nanotube lengths: **a** First mode, **b** Second mode, **c** Third mode, **d** Fourth mode

Overall, the torsional response results from the interplay of damping, scale effects, and structural parameters, emphasizing the need for moderate damping to achieve stable and physically meaningful predictions.

Acknowledgements The first author would like to thank for the scholarship provided by the Turkish Higher Education Council TÜBİTAK 2211A during his PhD.

Funding Open access funding provided by the Scientific and Technological Research Council of Türkiye (TÜBİTAK).

Data availability No data was used for the research described in the article.

Declarations

Conflict of interest The authors have no competing interests to declare that are relevant to the content of this article.

Open Access This article is licensed under a Creative Commons Attribution 4.0 International License, which permits use, sharing, adaptation, distribution and reproduction in any medium or format, as long as you give appropriate credit to the original author(s) and the source, provide a link to the Creative Commons licence, and indicate if changes were made. The images or other third party material in this article are included in the article's Creative Commons licence, unless indicated otherwise in a credit line to the material. If material is not included in the article's Creative Commons licence and your intended use is not permitted by statutory regulation or exceeds the permitted use, you will need to obtain permission directly from the copyright holder. To view a copy of this licence, visit http://creativecommons.org/licenses/by/4.0/.

References

1. A.C. Eringen, Nonlocal polar elastic continua. Int. J. Eng. Sci. **10**, 1–16 (1972). https://doi.org/10.1016/0020-7225(72)90070-5
2. V.T. Granik, Microstructural mechanics of granular media, Technique Report IM/MGU 78–241, Institute of Mechanics of Moscow State University, (1978)

3. V.T. Granik, M. Ferrari, Microstructural mechanics of granular media. Mech. Mater. **15**, 301–322 (1993). https://doi.org/10.1016/0167-6636(93)90005-C
4. M. Ferrari, V. Granik, A. Imam, J. Nadeau, Adv. Doublet Mech. (1997)
5. M. Kojic, I. Vlastelica, P. Decuzzi, V.T. Granik, M. Ferrari, A finite element formulation for the doublet mechanics modeling of microstructural materials. Comput. Methods Appl. Mech. Eng. **200**, 1446–1454 (2011). https://doi.org/10.1016/j.cma.2011.01.001
6. A. Fatahi-Vajari, A. Imam, Axial vibration of single-walled carbon nanotubes using doublet mechanics. Indian J. Phys. **90**, 447–455 (2016). https://doi.org/10.1007/s12648-015-0775-8
7. A. Fatahi-Vajari, A. Imam, Torsional vibration of single-walled carbon nanotubes using doublet mechanics. Z. Angew. Math. und Phys. **67**, 1–22 (2016). https://doi.org/10.1007/s00033-016-0675-6
8. M.A. Eltaher, N. Mohamed, Nonlinear stability and vibration of imperfect CNTs by doublet mechanics. Appl. Math. Comput. **382**, 125311 (2020). https://doi.org/10.1016/j.amc.2020.125311
9. M.Ö. Yayli, E. Asa, Longitudinal vibration of carbon nanotubes with elastically restrained ends using doublet mechanics. Microsyst. Technol. **26**, 499–508 (2020). https://doi.org/10.1007/s00542-019-04512-1
10. Ö. Civalek, B. Uzun, M.Ö. Yayli, Buckling analysis of nanobeams with deformable boundaries via doublet mechanics. Arch. Appl. Mech. **91**, 4765–4782 (2021). https://doi.org/10.1007/s00419-021-02032-x
11. Ö. Civalek, B. Uzun, M.Ö. Yaylı, Longitudinal vibration analysis of FG nanorod restrained with axial springs using doublet mechanics. Waves Random Complex Media **34**, 4937–4959 (2024). https://doi.org/10.1080/17455030.2021.2000675
12. Ö. Civalek, B. Uzun, M.Ö. Yaylı, An eigenvalue solution for torsional vibrations of restrained porous nanorods using doublet mechanics theory. J. Braz. Soc. Mech. Sci. Eng. **44**, 1–15 (2022). https://doi.org/10.1007/s40430-022-03415-z
13. M.R. Ebrahimian, A. Imam, M. Najafi, The effect of chirality on the torsion of nanotubes embedded in an elastic medium using doublet mechanics. Indian J. Phys. **94**, 31–45 (2020). https://doi.org/10.1007/s12648-019-01455-1
14. Z. Azimzadeh, A. Fatahi-Vajari, Coupled axial-radial vibration of single-walled carbon nanotubes via doublet mechanics. J. Solid Mech. **11**, 323–340 (2019). https://doi.org/10.22034/JSM.2019.665256
15. H.G. Kadıoğlu, M.Ö. Yaylı, Analysis of torsional vibration in viscoelastic functionally graded nanotubes with viscoelastic constraints using doublet mechanics theory. Int. J. Mech. Mater. Des. **21**, 1811–1833 (2025). https://doi.org/10.1007/s10999-025-09802-3
16. M.A. Eltaher, N. Mohamed, S.A. Mohamed, Nonlinear buckling and free vibration of curved CNTs by doublet mechanics. Smart Struct. Syst. **26**, 213–226 (2020). https://doi.org/10.12989/sss.2020.26.2.213
17. A. Karamanli, Structural behaviours of zigzag and armchair nanobeams using finite element doublet mechanics. Eur. J. Mech. A/Solids. **89**, 104287 (2021). https://doi.org/10.1016/j.euromechsol.2021.104287
18. U. Gul, M. Aydogdu, Structural modelling of nanorods and nanobeams using doublet mechanics theory. Int. J. Mech. Mater. Des. **14**, 195–212 (2018). https://doi.org/10.1007/s10999-017-9371-8
19. U. Gul, M. Aydogdu, Noncoaxial vibration and buckling analysis of embedded double-walled carbon nanotubes by using doublet mechanics. Compos. Part B Eng. **137**, 60–73 (2018). https://doi.org/10.1016/j.compositesb.2017.11.005
20. U. Gul, M. Aydogdu, Vibration analysis of Love nanorods using doublet mechanics theory. J. Braz. Soc. Mech. Sci. Eng. **41**, 1–12 (2019). https://doi.org/10.1007/s40430-019-1849-x
21. U. Gul, M. Aydogdu, A micro/nano-scale Timoshenko-Ehrenfest beam model for bending, buckling and vibration analyses based on doublet mechanics theory. Eur. J. Mech. A/Solids. **86**, 104199 (2021). https://doi.org/10.1016/j.euromechsol.2020.104199
22. U. Gul, M. Aydogdu, Buckling analysis of functionally graded beams with periodic nanostructures using doublet mechanics theory. J. Braz. Soc. Mech. Sci. Eng. **43**, 1–8 (2021). https://doi.org/10.1007/s40430-021-02972-z
23. U. Gul, M. Aydogdu, Transverse wave propagation analysis in single-walled and double-walled carbon nanotubes via higher-order doublet mechanics theory. Waves Random Complex Media **33**, 762–793 (2023). https://doi.org/10.1080/17455030.2021.1959085
24. U. Gul, M. Aydogdu, Vibration of layered nanobeams with periodic nanostructures. Mech. Based Des. Struct. Mach. **51**, 620–641 (2023). https://doi.org/10.1080/15397734.2020.1848592
25. U. Gul, M. Aydogdu, Finite element analysis for longitudinal vibration of nanorods based on doublet mechanics. Adv. Nano Res. **15**, 411–422 (2023). https://doi.org/10.12989/anr.2023.15.5.411
26. U. Gul, M. Aydogdu, Dynamic analysis of functionally graded beams with periodic nanostructures. Compos. Struct. **257**, 113169 (2021). https://doi.org/10.1016/j.compstruct.2020.113169
27. U. Gul, M. Aydogdu, Hygro-thermal vibration behavior of porous functionally graded nanobeams based on doublet mechanics. Arch. Mech. **76**, 413–450 (2024). https://doi.org/10.24423/aom.4522
28. M. Aydogdu, U. Gul, Longitudinal vibration of double nanorod systems using doublet mechanics theory. Struct. Eng. Mech. **73**, 37–52 (2020). https://doi.org/10.12989/sem.2020.73.1.037
29. M. Aydogdu, U. Gul, Buckling analysis of double nanofibers embeded in an elastic medium using doublet mechanics theory. Compos. Struct. **202**, 355–363 (2018). https://doi.org/10.1016/j.compstruct.2018.02.015
30. U. Gul, M. Aydogdu, A softening-hardening nanomechanics theory for the static and dynamic analyses of nanorods and nanobeams: doublet mechanics. In: Modern Trends in Structural and Solid Mechanics 2: Vibrations (wiley, 2021), pp. 43–78
31. U. Gul, M. Aydogdu, G. Gaygusuzoglu, Vibration and buckling analysis of nanotubes (nanofibers) embedded in an elastic medium using doublet Mechanics. J. Eng. Math. **109**, 85–111 (2018). https://doi.org/10.1007/s10665-017-9908-8
32. U. Gul, M. Aydogdu, G. Gaygusuzoglu, Axial dynamics of a nanorod embedded in an elastic medium using doublet mechanics. Compos. Struct. **160**, 1268–1278 (2017). https://doi.org/10.1016/j.compstruct.2016.11.023
33. M.R. Ebrahimian, A. Imam, M. Najafi, Doublet mechanical analysis of bending of Euler-Bernoulli and Timoshenko nanobeams. ZAMM Z. Angew. Math. Mech. **98**, 1642–1665 (2018). https://doi.org/10.1002/zamm.201700365
34. H. Koc, E. Tufekci, A novel approach of bending behavior of carbon nanotubes by combining the effects of higher-order boundary conditions and coupling through doublet mechanics. Mech. Adv. Mater. Struct. **31**, 8905–8919 (2024). https://doi.org/10.1080/15376494.2023.2263767
35. H. Koç, E. Tufekci, Analytical bending solutions for carbon nanotubes: paradoxes and their resolutions through doublet mechanics. Arch. Appl. Mech. **95**, 275 (2025). https://doi.org/10.1007/s00419-025-02970-w
36. M. Arefi, E. Mohammad-Rezaei Bidgoli, O. Civalek, Bending response of FG composite doubly curved nanoshells with thickness stretching via higher-order sinusoidal shear theory. Mech. Based Des. Struct. Mach. **50**, 2350–2378 (2022). https://doi.org/10.1080/15397734.2020.1777157
37. A. Fatahi-Vajari, A. Imam, Analysis of radial breathing mode of vibration of single-walled carbon nanotubes via doublet mechanics. ZAMM Z. Angew. Math. Mech. **96**, 1020–1032 (2016). https://doi.org/10.1002/zamm.201500160
38. R.R. Rout, R. Ranjan Dash, M.K. Padhy, Free vibration analysis of functionally graded nanobeams using doublet mechanics theory. Res. Dev. Mach. Des. **5**, 1–15 (2022)

39. M. Akpınar, B. Uzun, M.Ö. Yaylı, Dynamics of a nanotube supported on the lateral and rotational restrained using doublet mechanics theory. Acta Mech. **236**, 809–836 (2025). https://doi.org/10.1007/s00707-024-04173-w
40. A. Karamanli, T.P. Vo, Free vibration of axially loaded zigzag and armchair nanobeams using doublet mechanics. Mech. Based Des. Struct. Mach. **51**, 5808–5833 (2023). https://doi.org/10.1080/15397734.2021.2013878
41. R. Selvamani, T. Prabhakaran, M. Yaylacı, ŞE. Kartal, E.U. Yaylacı, Doublet structural modeling of nonhomogeneous Euler mass sensor nanobeams using boundary characteristics Bernstein polynomials. ZAMM Z. Angew. Math. Mech. **105**, e202401264 (2025). https://doi.org/10.1002/zamm.202401264
42. A. Fatahi-Vajari, A new method for evaluating the natural frequency in radial breathing like mode vibration of double-walled carbon nanotubes. ZAMM Z. Angew. Math. Mech. **98**, 255–269 (2018). https://doi.org/10.1002/zamm.201600234
43. A. Karamanli, T.P. Vo, Finite element model for free vibration analysis of curved zigzag nanobeams. Compos. Struct. **282**, 115097 (2022). https://doi.org/10.1016/j.compstruct.2021.115097
44. R. Selvamani, T. Prabhakaran, F. Ebrahimi, Doublet structural dynamics of porous Euler mass sensor nanobeam with Klein-Gordon nonlocality. Mech. Solids **60**, 2048–2069 (2025). https://doi.org/10.1134/S0025654425600722
45. A. Karamanli, N.D. Nguyen, S. Lee, T.P. Vo, Improved FSDT for forced vibration analysis of nanobeams under moving concentrated loads via doublet mechanics. Mech. Based Des. Struct. Mach. (2025). https://doi.org/10.1080/15397734.2025.2548857
46. R. Özmen, I. Esen, Dynamic response of embedded Timoshenko CNTs exposed to magnetic and thermal fields subjected to moving load based on doublet mechanics. J. Braz. Soc. Mech. Sci. Eng. **45**, 1–19 (2023). https://doi.org/10.1007/s40430-023-04506-1
47. A.A. Abdelrahman, R.A. Shanab, I. Esen, M.A. Eltaher, Effect of moving load on dynamics of nanoscale Timoshenko CNTs embedded in elastic media based on doublet mechanics theory. Steel Compos. Struct. **44**, 255–270 (2022). https://doi.org/10.12989/scs.2022.44.2.255
48. F. Mehralian, Y.T. Beni, Size-dependent torsional buckling analysis of functionally graded cylindrical shell. Compos. Part B Eng. **94**, 11–25 (2016). https://doi.org/10.1016/j.compositesb.2016.03.048
49. B. Akgoz, O. Civalek, Buckling analysis of linearly tapered micro-columns based on strain gradient elasticity. Struct. Eng. Mech. **48**, 195–205 (2013). https://doi.org/10.12989/sem.2013.48.2.195
50. S.K. Jena, S. Chakraverty, R.M. Jena, Stability analysis of Timoshenko nanobeam with material uncertainties using a double-parametric form-based analytical approach and Monte Carlo simulation technique. Eur. Phys. J. Plus. **135**, 536 (2020). https://doi.org/10.1140/epjp/s13360-020-00549-8
51. Y. Tadi Beni, Size dependent torsional electro-mechanical analysis of flexoelectric micro/nanotubes. Eur. J. Mech. A/Solids. **95**, 104648 (2022). https://doi.org/10.1016/j.euromechsol.2022.104648
52. Y. Tadi Beni, Size dependent coupled electromechanical torsional analysis of porous FG flexoelectric micro/nanotubes. Mech. Syst. Signal Process. **178**, 109281 (2022). https://doi.org/10.1016/j.ymssp.2022.109281
53. M.M. Selim, M.F. Alotaibi, A. Soltani, A.B.A. Mohamed, A.H. Abdel-Aty, Torsional vibrational analysis of irregular single-walled carbon nanotube with elastic-support boundary conditions. J. Mater. Res. Technol. **24**, 215–222 (2023). https://doi.org/10.1016/j.jmrt.2023.02.230
54. A. Fatahi-Vajari, Z. Azimzadeh, Axial vibration of single-walled carbon nanotubes with fractional damping using doublet mechanics. Indian J. Phys. **94**, 975–986 (2020). https://doi.org/10.1007/s12648-019-01547-y
55. A. Fatahi-Vajari, Z. Azimzadeh, Analysis of nonlinear axial vibration of single-walled carbon nanotubes using homotopy perturbation method. Indian J. Phys. **92**, 1425–1438 (2018). https://doi.org/10.1007/s12648-018-1203-7
56. U. Gul, Dynamic analysis of short-fiber reinforced composite nanobeams based on nonlocal strain gradient theory. Proc. Inst. Mech. Eng. Part C J. Mech. Eng. Sci. **238**, 2641–2676 (2024). https://doi.org/10.1177/09544062241227086
57. B. Uzun, Magnetic field and non-local effects on axial vibration of embedded nanorods reinforced with short fibers. Acta Mech. **236**, 4889–4920 (2025). https://doi.org/10.1007/s00707-025-04417-3
58. M. Akpınar, B. Uzun, M.Ö. Yaylı, Size-dependent dynamics of perforated and short-fiber-reinforced nanowires based on non-local modified couple stress theory. J. Vib. Eng. Technol. **13**, 1–18 (2025). https://doi.org/10.1007/s42417-024-01662-z
59. Ö. Civalek, B. Uzun, M.Ö. Yaylı, Torsional static and free vibration analysis of noncircular short-fiber-reinforced microwires with arbitrary boundary conditions. Polym. Compos. **46**, 971–985 (2025). https://doi.org/10.1002/pc.27321
60. M. Akpınar, B. Uzun, M.Ö. Yaylı, Nonlocal elasticity-based torsional vibration analysis of short-fiber-reinforced nanorods with elliptical and triangular cross-sections. Int. J. Mech. Mater. Des. **22**, 87 (2026). https://doi.org/10.1007/s10999-026-09906-4
61. M. Sobhy, A.M. Zenkour, Magnetic field effect on thermomechanical buckling and vibration of viscoelastic sandwich nanobeams with CNT reinforced face sheets on a viscoelastic substrate. Compos. Part B Eng. **154**, 492–506 (2018). https://doi.org/10.1016/j.compositesb.2018.09.011
62. Y. Zhang, Y. Li, G. Zhang, X. Zhang, Nonlinear bending of FG-CNTR curved nanobeams in thermal environments. Acta Mech. Solida Sin. **38**, 166–180 (2024). https://doi.org/10.1007/s10338-024-00524-1
63. Ö. Civalek, S. Dastjerdi, ŞD. Akbaş, B. Akgöz, Vibration analysis of carbon nanotube-reinforced composite microbeams. Math. Methods Appl. Sci. (2021). https://doi.org/10.1002/MMA.7069
64. M. Alimoradzadeh, D. Akbaş, Nonlinear oscillations of a composite microbeam reinforced with carbon nanotube based on the modified couple stress theory. Coupled Syst. Mech. **11**, 485–504 (2022). https://doi.org/10.12989/csm.2022.11.6.485
65. I. Esen, A.A. Daikh, M.A. Eltaher, Dynamic response of nonlocal strain gradient FG nanobeam reinforced by carbon nanotubes under moving point load. Eur. Phys. J. Plus. **136**, 1–22 (2021). https://doi.org/10.1140/epjp/s13360-021-01419-7
66. K. Arshadi, M. Arefi, Out-of-plane strain included formulation for free vibration and bending analyses of a sandwich GPL-reinforced microbeam based on the MCST. J. Vib. Eng. Technol. **11**, 2199–2214 (2023). https://doi.org/10.1007/s42417-022-00698-3
67. E. Mohammad-Rezaei Bidgoli, M. Arefi, Size-dependent thermomechanical critical loads of GPL-reinforced nanobeams. Waves Random Complex Media (2023). https://doi.org/10.1080/17455030.2023.2169385
68. M. Arefi, E.M.-R. Bidgoli, R. Dimitri, F. Tornabene, J.N. Reddy, Size-dependent free vibrations of FG polymer composite curved nanobeams reinforced with graphene nanoplatelets resting on pasternak foundations. Appl. Sci. **9**, 1580 (2019). https://doi.org/10.3390/app9081580
69. G. Manickam, P. Gupta, S. De, V. Rajamohan, O. Polit, Nonlinear flexural free vibrations of size-dependent graphene platelets reinforced curved nano/micro beams by finite element approach coupled with trigonometric shear flexible theory. Mech. Adv. Mater. Struct. **29**, 2489–2515 (2022). https://doi.org/10.1080/15376494.2020.1866723
70. Y. Fang, Y.Y. Wang, Y.Q. Zhang, Bending and vibration analyses of graphene-reinforced functionally graded composite curved nanobeam with high-order surface effects. Acta Mech. **236**, 2425–2444 (2025). https://doi.org/10.1007/s00707-025-04287-9
71. X. Yang, H. Liu, J. Ma, Thermo-mechanical vibration of FG curved nanobeam containing porosities and reinforced by graphene platelets. Microsyst. Technol. **26**, 2535–2551 (2020). https://doi.org/10.1007/s00542-020-04794-w
72. M. Akpınar, B. Uzun, H.G. Kadıoğlu, M.Ö. Yaylı, Dynamic analysis of restrained short-fiber-reinforced and functionally graded nanobeams via stress-driven model. ZAMM Z. Angew. Math. Mech. **105**, 70133 (2025). https://doi.org/10.1002/zamm.70133

73. M. Botshekanan Dehkordi, Y.T. Beni, A. Cheraghbak, On the nonlocal nonlinear vibration of electro-magneto piezoelectric porous visco-microbeam reinforced with agglomerated CNTs considering surface effects. Appl. Phys. A Mater. Sci. Process. **130**, 1–17 (2024). https://doi.org/10.1007/s00339-024-08048-8
74. H.G. Kadıoğlu, B. Uzun, Ö. Civalek, M.Ö. Yaylı, Dynamic behavior of micromorphic viscoelastic Euler-Bernoulli beams under viscoelastic boundary constraints. Acta Mech. **236**, 4475–4490 (2025). https://doi.org/10.1007/s00707-025-04364-z
75. M. Arda, Vibration analysis of an axially loaded viscoelastic nanobeam. Int. J. Eng. Appl. Sci. **10**, 252–263 (2018). https://doi.org/10.24107/ijeas.468769
76. L. Wang, N. Chong, D. Lei, Z. Ou, Nonlinear vibration analysis of nonlocal fractional viscoelastic piezoelectric nanobeams incorporating surface effects. Eur. J. Mech. A/Solids. **115**, 105840 (2026). https://doi.org/10.1016/j.euromechsol.2025.105840
77. N. Chong, L. Wang, D. Lei, Z. Ou, Nonlinear vibration of fractional viscoelastic piezoelectric nanobeams based on nonlocal theory. Arch. Appl. Mech. **95**, 150 (2025). https://doi.org/10.1007/s00419-025-02859-8
78. A.E. Abouelregal, B. Akgöz, O. Civalek, Magneto-thermoelastic interactions in an unbounded orthotropic viscoelastic solid under the hall current effect by the fourth-order Moore-Gibson-Thompson equation. Comput. Math. with Appl. **141**, 102–115 (2023). https://doi.org/10.1016/j.camwa.2023.04.001
79. M. Arda, Torsional vibration analysis of carbon nanotubes using Maxwell and Kelvin-Voigt type viscoelastic material models. Eur. Mech. Sci. **4**, 90–95 (2020). https://doi.org/10.26701/ems.669495
80. A.H. Ghorbanpour-Arani, A. Rastgoo, M.M. Sharafi, R. Kolahchi, A. Ghorbanpour Arani, Nonlocal viscoelasticity based vibration of double viscoelastic piezoelectric nanobeam systems. Meccanica **51**, 25–40 (2016). https://doi.org/10.1007/s11012-014-9991-0
81. S. Ceballes, R. Quintana, A. Abdelkefi, Comparative analysis between surrounding viscoelastic media on the buckling characteristics of nanobeams. Microsyst. Technol. **27**, 3007–3024 (2021). https://doi.org/10.1007/s00542-020-05049-4
82. H.G. Kadıoğlu, M.Ö. Yaylı, Nonlocal viscoelastic medium approach to free vibrations of modified Jeffreys viscoelastic nanobeams. Int. J. Mech. Mater. Des. **22**, 10 (2026). https://doi.org/10.1007/s10999-025-09840-x
83. R. Guzmán de Villoria, A. Miravete, Mechanical model to evaluate the effect of the dispersion in nanocomposites. Acta Mater. **55**, 3025–3031 (2007). https://doi.org/10.1016/j.actamat.2007.01.007
84. N. Pan, Theoretical determination of the optimal fiber volume fraction and fiber-matrix property compatibility of short fiber composites. Polym. Compos. **14**, 85–93 (1993). https://doi.org/10.1002/pc.750140202

Publisher's Note Springer Nature remains neutral with regard to jurisdictional claims in published maps and institutional affiliations.